Path Integral Monte Carlo and Density Functional Molecular Dynamics Simulations of Hot, Dense Helium

B. Militzer
Departments of Earth and Planetary Science and Astronomy, University of California, Berkeley, CA 94720, USA
(Dated: February 25, 2009)

Two first-principles simulation techniques, path integral Monte Carlo (PIMC) and density functional molecular dynamics (DFT-MD), are applied to study hot, dense helium in the density-temperature range of 0.387 – 5.35 $\mathrm{g\,cm^{-3}}$ and 500 K – 1.28×10^8 K. One coherent equation of state (EOS) is derived by combining DFT-MD data at lower temperatures with PIMC results at higher temperatures. Good agreement between both techniques is found in an intermediate temperature range. For the highest temperatures, the PIMC results converge to the Debye-Hückel limiting law. In order to derive the entropy, a thermodynamically consistent free energy fit is introduced that reproduces the internal energies and pressure derived from the first-principles simulations. The equation of state is presented in the form of a table as well as a fit and is compared with different free energy models. Pair correlation functions and the electronic density of states are discussed. Shock Hugoniot curves are compared with recent laser shock wave experiments.

I. INTRODUCTION

After hydrogen, helium is the most common element in the universe. While it rarely occurs in pure form in nature, it is an endmember of hydrogen-helium mixtures (HHM) that are the prevalent component in solar and extrasolar giant gas planets. The characterization of helium's properties at extreme temperature and pressure conditions is therefore important for the study of planetary interiors and especially relevant for answering the question of whether HHM phase-separate in giant planet interiors[1,2]. In most planetary models, the equation of state (EOS) of HHM was inferred from the linear mixing approximation at constant pressure and temperature using the EOSs of pure hydrogen and helium. The latter is the central topic of this article.

Hydrogen and helium share some common properties. Both are very light and exhibit rich quantum properties at low temperature. More importantly for this paper, the helium atom and the deuterium molecule have similar masses and both have two elemental excitation mechanisms that determine their behavior at high temperature. The helium atom has two ionization stages while deuterium molecules can dissociate and the resulting atoms can be ionized. However, helium is without question simpler to characterize at high pressure. The crystal structure is hexagonal closed-packed under most (P,T) conditions[3,4] while in solid hydrogen, different degrees of molecular rotational ordering lead to several phases that deviate from the h.c.p. structure. Hydrogen is expected to turn metallic at a few hundred GPa while a much larger band gap must be closed in helium, which is predicted to occur at 11 200 GPa[5,6] according density functional theory (DFT) and at 25 700 GPa according to recent quantum Monte Carlo calculations[7]. The difference arises because standard DFT methods underestimate the band gap by 4 eV in dense solid helium.

Given the relative simplicity of helium's high pressure properties, one expects that there would be less of a controversy in the EOS than for hydrogen. This makes helium a good material to test novel experimental and theoretical approaches. For hydrogen, the results of first laser shock experiments that reached megabar pressures had predicted that the material would be highly compressible under shock conditions and reach densities six times higher than the initial state[8,9]. Later experiments[10–13] showed reduced compression ratios close to 4.3, which were in good agreement with first-principles calculations[14,15]. Good agreement between gas gun experiments by Holmes *et al.*[16] and first-principles simulations has also been demonstrated[17,18]. The same is true for helium where very good agreement between early gas gun experiments by Nellis *et al.*[19] and first-principles simulations has been found[20].

Recently the first laser shock experiments were performed on precompressed helium samples[21]. The measurements confirmed the theoretically predicted trend[20] that the shock compression ratio is reduced with increasing precompression. However, there is a discrepancy in the magnitude of the compression. Shock measurements[21] without precompression showed compression ratios of about 6 while first-principles simulation[20] predicted only 5.24(4). The discrepancy between theoretical and experimental predictions is reduced for higher precompressions. For samples that were precompressed to 3.4-fold the ambient density, theory and experiment are in agreement.

The properties of fluid helium change from hard-sphere liquid at low pressure and temperature to ultimately a two-component plasma, after ionization has occurred at high pressure and temperature. The associated insulator-to-metal transition has been the topic of three recent theoretical studies that all relied on DFT methods. Kietzmann *et al.*[22] studied the rise in electrical conductivity using the Kubo-Greenwood formula and compared with results of shock-wave experiments by Ternovoi *et al.*[23]. Kowalski *et al.*[6] studied dense helium in order to characterize the atmosphere of white dwarfs. This paper

went beyond the generalized gradient approximation by considering hybrid functionals. Stixrude and Jeanloz[24] studied the band gap closure in the dense fluid helium over a wide range of densities including conditions of giant planet interiors. Two recent studies of Jupiter's interior[25,26], to different extent, relied on a helium EOS derived from DFT-MD.

This article provides the EOS for fluid helium over a wide range of temperatures (500 K–1.28×10^8 K) and densities (0.387–5.35 g cm^{-3} corresponding to a Wigner-Seitz radius interval of r_s=2.4–1.0 where $\frac{4}{3}\pi r_s^3 = V/N_e$) by combining two first-principles simulation methods, path integral Monte Carlo (PIMC) at higher temperatures and density functional molecular dynamics (DFT-MD) at lower temperatures. PIMC is very efficient at high temperature but becomes computationally more demanding with decreasing temperature because the length of the path scale like $1/T$. DFT is a very efficient groundstate method but with increasing temperature more and more unoccupied orbitals need to be included, which eventually adds considerably to the computational cost.

The temperature range of the PIMC simulations was significantly extended compared to our earlier work[20] that focused exclusively on shock properties alone. Here, the region of validity of both first-principles methods is analyzed and good agreement for EOS at intermediate temperatures is demonstrated. The PIMC calculations are extended to much higher temperatures until good agreement with the Debye-Hückel limiting law is found. In the density interval under consideration, the entire EOS of nonrelativistic, fluid helium has been mapped out from first principles. All EOS data are combined into one thermodynamically consistent fit for the free energy, and the entropy is derived. The structure of the fluid is analyzed using pair correlation functions and, finally, additional results for shock Hugoniot curves are presented.

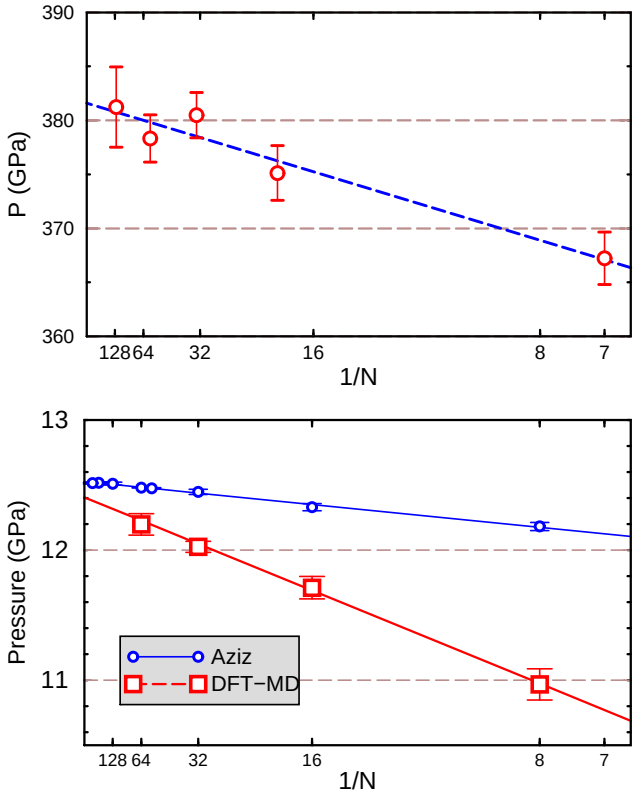

FIG. 1: The upper panel shows the finite size dependence of the pressure as function of the number atoms, N, as predicted from PIMC simulations with free-particle nodes at T=125 000 K and $r_s = 1.86$. The lower panel compares the finite size dependence of DFT-MD simulations and classical Monte Carlo calculations using the Aziz pair potential at T=10 000 K and $r_s = 2.4$.

II. METHODS

Path integral Monte Carlo[27] is the most appropriate and efficient first-principles simulation techniques for a quantum system at finite temperature. Electrons and nuclei are treated equally as paths, although the zero-point motion of the nuclei as well as exchange effects are negligible for the temperatures under consideration. The Coulomb interaction between electrons and nuclei is introduced using pair density matrices that we derived using the eigenstates of the two-body Coulomb problem[28]. The periodic images were treated using an optimized Ewald break-up[29] that we applied to the pair action[30]. PIMC includes all correlation effects, which for example leads an exact treatment of the isolated helium atom.

PIMC simulations with more two electrons in a dense system suffer from a fermion sign problem, which is the result of the near complete cancellation of positive and negative contributions to the many-body density matrix in degenerate fermionic systems. In groundstate quantum Monte Carlo methods[31], this problem is solved by introducing the fixed node approximation where walkers are prohibited from enter negative regions of a trial wave function, $\Psi_T(\mathrm{R}) > 0$. Most often Ψ_T is represented by a Slater determinant filled with single particle orbitals derived with the Hartree-Fock method or from density functional theory. Recent studies found significant improvements by considering backflow wave functions[32,33] and Pfaffians[34].

The fixed node approximation in fermionic PIMC[35,36] is more complicated because one not only needs an analytical approximation to the groundstate wave function but to the many-body density matrix, $\rho_T(\mathbf{R},\mathbf{R}';\beta)$, over a range of temperatures, $T = 1/\beta$,

$$\rho_F(\mathbf{R},\mathbf{R}';\beta) = \frac{1}{N!}\sum_{\mathcal{P}}(-1)^{\mathcal{P}}\int_{\substack{\mathbf{R}\to\mathcal{P}\mathbf{R}'\\ \rho_T(\mathbf{R},\mathbf{R}_t;t)>0}} \mathbf{dR}_t\ e^{-S[\mathbf{R}_t]}, \quad (1)$$

The action, $S[\mathbf{R}_t]$, determines the weight of every path. The nodal restriction, $\rho_T(\mathbf{R},\mathbf{R}_t;t) > 0$, is enforced at

every point on the path, $\mathbf{R} \rightarrow \mathcal{P}\mathbf{R}'$, and guarantees that only positive contributions from the sum over permutations, $\mathcal{P}$, enter when diagonal elements of density matrix elements, $\rho_F(\mathbf{R}, \mathbf{R}' = \mathbf{R}; \beta)$, are computed. In general observables are derived from,

$$\left\langle \hat{O} \right\rangle = \frac{\int \mathbf{dR} \int \mathbf{dR}' \, \langle \mathbf{R}| \, \hat{O} \, |\mathbf{R}'\rangle \, \rho_F(\mathbf{R}', \mathbf{R}; \beta)}{\int \mathbf{dR} \, \rho_F(\mathbf{R}, \mathbf{R}; \beta)} \qquad (2)$$

but for the internal, kinetic, and potential energy as well as for the pressure and pair correlation functions, but not for the momentum distribution, diagonal elements are sufficient[27], which means all PIMC simulation for this study were performed with closed paths, $\mathbf{R} \rightarrow \mathcal{P}\mathbf{R}$.

The most common approximation to the trial density matrix is a Slater determinant of single particle density matrices,

$$\rho_T(\mathbf{R}, \mathbf{R}'; \beta) = \begin{vmatrix} \rho^{[1]}(\mathbf{r}_1, \mathbf{r}'_1; \beta) & \dots & \rho^{[1]}(\mathbf{r}_N, \mathbf{r}'_1; \beta) \\ \dots & \dots & \dots \\ \rho^{[1]}(\mathbf{r}_1, \mathbf{r}'_N; \beta) & \dots & \rho^{[1]}(\mathbf{r}_N, \mathbf{r}'_N; \beta) \end{vmatrix} . \qquad (3)$$

The free particle nodal structure is obtained by entering the density matrices of noninteracting particles,

$$\rho_0^{[1]}(\mathbf{r}, \mathbf{r}'; \beta) = (4\pi\lambda\beta)^{-d/2} \exp\left\{ -\frac{(\mathbf{r} - \mathbf{r}')^2}{4\lambda\beta} \right\} \quad , \qquad (4)$$

with $\lambda = \hbar^2/2m$, which becomes exact in the limit of high temperature. The variational density matrix (VDM) approach[37] is currently the only available technique that goes beyond free particle nodal approximation by including interaction effects into the PIMC nodal structure. This approach is more accurate but also more demanding computationally. Most results in this article will be derived with free particle nodes but some comparisons with VDM nodes will be presented.

The DFT-MD simulations were performed with either the CPMD code[38] using local Troullier-Martins norm-conserving pseudopotentials[39] or with the Vienna ab initio simulation package[40] using the projector augmented-wave method[41]. Exchange-correlation effects were described by the Perdew-Burke-Ernzerhof generalized gradient approximation[42]. The electronic wave functions were expanded in a plane-wave basis with energy cut-off of 30-50 Hartrees. Most simulations were performed with N=64 using Γ point sampling of the Brillioun zone. An analysis of finite size effect is presented in the following section.

The nuclei were propagated using Born-Oppenheimer molecular dynamics with forces derived from either the electronic ground state or by including a thermal population of unoccupied electronic orbitals[43] when they make nonneglible contributions to the energy or pressure in thermodynamic equilibrium at elevated temperatures. By comparing with PIMC, it will be demonstrated that the thermal population of unoccupied Kohn-Sham orbitals leads to an accurate description of the EOS at high temperature and density. This extends the applicability range of DFT, which was developed as a ground-state electronic structure method.

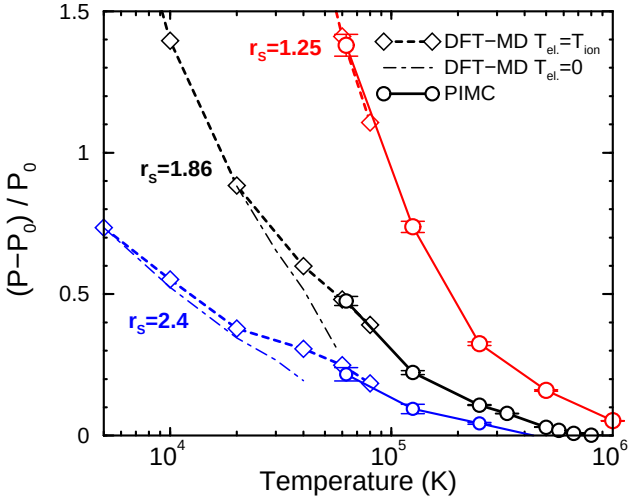

FIG. 2: Comparison of the relative excess pressure derived from PIMC (solid lines) and DFT-MD. The dashed and the dash-dotted lines show results from DFT-MD simulations using electronic groundstate and for $T_{\rm el} = T_{\rm ion}$, respectively.

III. EQUATION OF STATE

An analysis of finite size dependence of the EOS results is important since all simulations are performed with a finite number of particles under periodic boundary conditions. Figure 1 gives two examples for the finite size analysis that we have performed at various temperature and density conditions. At 10 000 K and $r_s = 2.4$, helium can be characterized as a hard-sphere fluid. The artificial periodicity of the nuclei dominate the finite size errors. Simulations with $N = 64$ atoms are sufficiently accurate for the purpose of this study. The DFT-MD results also agree surprisingly well with classical Monte Carlo calculation using the Aziz pair potential[44], which explains why both methods give fairly similar Hugoniot curves as long as thermal electronic excitations are not important[20].

The upper panel of Fig. 1 shows PIMC results for 125 000 K where a substantial part of the pressure comes from the thermally excited electrons. They are still coupled to the motion of the nuclei, which leads to effective screening. In consequence, the finite size dependence of the pressure is reduced significantly, and a simulation with $N = 16$ atoms exhibits a finite size error of only 1% compared with 3% at lower temperature. This is the reason why PIMC simulations with 16 atoms already give a fairly accurate shock Hugoniot curve[20]. However, most PIMC results reported in Tab. I were obtained with 32 atoms and some with 57 atoms. Already 32 atoms lead to well converged pressures unless one is interested in very

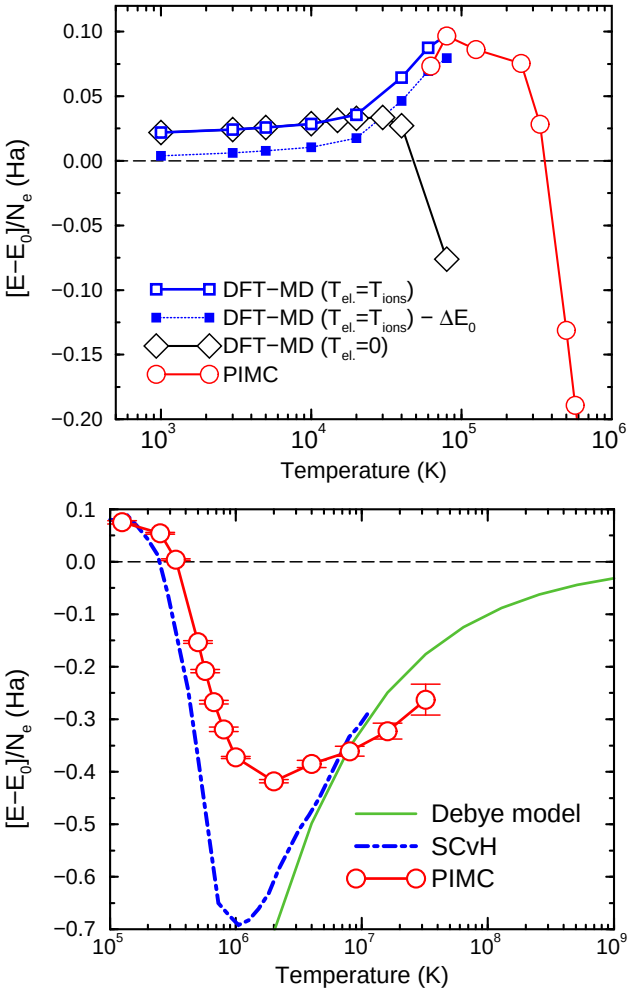

FIG. 3: Excess internal energy per electron relative to the ideal plasma model at a density of r_s=1.86. The circles show PIMC results. In the upper panel, the open squares and diamonds show DFT-MD results using the electronic ground-state and for $T_{\rm el} = T_{\rm ion}$, respectively. The filled squares shows DFT-MD results corrected by constant shift corresponding to the DFT error of the isolated helium atom. In lower panel, PIMC results are compared with the Debye model.

high temperatures, above 10^7K, where all atoms are ionized and the coupling is very weak. Although the total pressure is dominated by the kinetic term, the accurate determination of the small contribution from the interactions shows an increased finite size dependence that requires simulation with 57 atoms in some cases. In general, the weak-coupling limit is difficult to study with finite-size simulations[45,46]. Also at very high density, beyond the range considered here, electrons approach the limit of an ideal Fermi gas and form a rigid background. The remaining Coulombic subsystem of ions is expected to require simulations with several hundreds of particles[47]. In this regard, the electronic screening makes our simulations affordable.

Figure 2 compares the pressures obtained from PIMC and DFT-MD simulations for several densities. At r_s = 1.86, thermal population of unoccupied electronic states becomes important above 20 000 K. Both first-principles method are in very good agreement, which is the foundation for the coherent EOS reported in this paper. Reasonably good agreement between PIMC and DFT-MD was reported for hydrogen earlier[48]. Figure 2 is a stringent test because it compares only the pressure contributions that result from the particle interactions. When one removes the ideal gas contributions, P_0, one has a bit of a choice for the corresponding noninteracting system. At very high temperature, one wants to compare with an ideal Fermi gas of electrons and nuclei. At low temperature, however, comparing with a gas of noninteracting atoms is preferred. To combine these to limiting cases, we construct a simple chemical model that includes neutral atoms, He^+ and He^{2+} ions as well as free electrons. The ionization state is derived from the Saha equilibrium using the following binding energies, $E_{\rm He} = -2.9037$ Ha, $E_{\rm He+} = -2$ Ha. Besides the binding energies, no other interactions are considered.

TABLE I: EOS table with pressures, internal and free energies per electron derived from (a) DFT-MD with 64 atoms (a uniform $\Delta E/N_e = -0.01919$ Ha correction was added to account for missing DFT correlation energy in the helium atom), PIMC with (b) 32 atoms, (c) PIMC with 57 atoms, and (d) Debye-Hückel limiting law. The numbers in brackets indicate the statistical uncertainties of the DFT-MD and PIMC simulations for the corresponding number trailing digits.

r_s	T(K)	P (GPa)	E/N_e (Ha)	F/N_e (Ha)
2.4[a]	500	1.420(10)	-1.449873(7)	-1.4554
2.4[a]	1000	2.045(14)	-1.448401(10)	-1.46135
2.4[a]	3000	4.69(3)	-1.44273(3)	-1.49126
2.4[a]	5000	6.98(4)	-1.43727(3)	-1.52534
2.4[a]	10000	12.49(4)	-1.42395(5)	-1.61873
2.4[a]	20000	22.19(8)	-1.39427(12)	-1.82386
2.4[a]	40000	43.37(11)	-1.2997(2)	-2.28643
2.4[a]	60000	68.27(10)	-1.1748(2)	-2.80627
2.4[a]	80000	96.93(12)	-1.02525(7)	-3.37236
2.4[b]	125000	172.3(6)	-0.6667(17)	-4.77369
2.4[b]	250000	445.7(6)	0.477(2)	-9.31702
2.4[b]	333333	651.4(9)	1.237(3)	-12.6707
2.4[b]	500000	1067.7(1.0)	2.634(3)	-19.922
2.4[b]	571428	1249.9(9)	3.216(3)	-23.1952
2.4[b]	666667	1484.2(5)	3.9507(16)	-27.6612
2.4[b]	800000	1815.5(1.2)	4.972(4)	-34.0708
2.4[b]	1×10^6	2308.4(7)	6.470(2)	-43.9954
2.4[b]	2×10^6	4745.2(8)	13.754(2)	-97.4249
2.4[b]	4×10^6	9587.6(1.2)	28.102(4)	-213.949
2.4[d]	8×10^6	19253	56.72	-466.803
2.4[d]	16×10^6	38577	113.80	-1013.36
2.4[d]	32×10^6	77205	227.87	-2184.48
2.4[d]	64×10^6	154445	455.92	-4683.43
2.4[d]	128×10^6	308916	911.97	-10002.6
2.4[d]	256×10^6	617849	1824.04	-21267.5
2.4[d]	512×10^6	1235711	3648.14	-45052.4
2.4[d]	1024×10^6	2471430	7296.32	-95193.5
2.4[d]	2048×10^6	4942866	14592.67	-200489

TABLE II: Table I continued.

r_s	T(K)	P (GPa)	E/N_e (Ha)	F/N_e (Ha)
2.2[a]	500	2.74(2)	-1.449495(13)	-1.45451
2.2[a]	1000	3.77(3)	-1.44787(2)	-1.4601
2.2[a]	3000	7.59(3)	-1.44186(2)	-1.48855
2.2[a]	5000	10.81(6)	-1.43615(3)	-1.5214
2.2[a]	10000	18.23(7)	-1.42256(5)	-1.61205
2.2[a]	20000	31.39(7)	-1.39256(9)	-1.812
2.2[a]	40000	59.54(13)	-1.30036(19)	-2.2635
2.2[a]	60000	92.10(11)	-1.17937(16)	-2.77064
2.2[a]	80000	129.52(10)	-1.03399(12)	-3.32222
2.2[b]	125000	223.9(7)	-0.6962(16)	-4.68439
2.2[b]	250000	569.6(7)	0.3971(16)	-9.08923
2.2[b]	500000	1371.3(6)	2.5403(14)	-19.3777
2.2[b]	1×10^6	2981.1(7)	6.3896(17)	-42.807
2.2[b]	2×10^6	6148.3(8)	13.694(2)	-95
2.2[b]	4×10^6	12438.6(1.7)	28.059(4)	-209.039
2.2[d]	8×10^6	24982	56.67	-456.924
2.2[d]	16×10^6	50075	113.77	-993.605
2.2[d]	32×10^6	100227	227.85	-2144.93
2.2[d]	64×10^6	200508	455.91	-4604.15
2.2[d]	128×10^6	401053	911.96	-9843.99
2.2[d]	256×10^6	802134	1824.03	-20951.2
2.2[d]	512×10^6	1604287	3648.13	-44420.5
2.2[d]	1024×10^6	3208587	7296.31	-93928.4
2.2[d]	2048×10^6	6417184	14592.66	-197960
2[a]	500	6.101(13)	-1.448584(6)	-1.45297
2[a]	1000	7.59(2)	-1.446835(11)	-1.45806
2[a]	3000	13.57(5)	-1.44022(3)	-1.48466
2[a]	5000	18.07(7)	-1.43433(4)	-1.51606
2[a]	10000	28.62(11)	-1.42013(8)	-1.60363
2[a]	20000	47.02(12)	-1.38968(11)	-1.79771
2[a]	40000	84.72(12)	-1.30039(15)	-2.23673
2[a]	60000	128.66(14)	-1.18357(12)	-2.72986
2[a]	80000	178.84(19)	-1.0433(2)	-3.26574
2[b]	125000	297.4(7)	-0.7291(12)	-4.58614
2[b]	250000	745.9(7)	0.3112(13)	-8.84403
2[b]	500000	1800.9(8)	2.4269(14)	-18.7895
2[b]	1×10^6	3941.2(1.0)	6.2898(17)	-41.5111
2[b]	2×10^6	8163.1(1.5)	13.621(3)	-92.3417
2[b]	4×10^6	16544(2)	28.009(4)	-203.653
2[d]	8×10^6	33228	56.61	-446.089
2[d]	16×10^6	66633	113.73	-971.926
2[d]	32×10^6	133390	227.82	-2101.53
2[d]	64×10^6	266868	455.88	-4517.11
2[d]	128×10^6	533797	911.95	-9669.7
2[d]	256×10^6	1067636	1824.02	-20604.1
2[d]	512×10^6	2135303	3648.12	-43727.2
2[d]	1024×10^6	4270628	7296.31	-92540.1
2[d]	2048×10^6	8541271	14592.66	-195186

TABLE III: Table II continued.

r_s	T(K)	P (GPa)	E/N_e (Ha)	F/N_e (Ha)
1.86[a]	1000	13.55(3)	-1.445347(12)	-1.45574
1.86[a]	3000	21.50(8)	-1.43837(4)	-1.48081
1.86[a]	5000	28.04(9)	-1.43196(4)	-1.51097
1.86[a]	10000	41.40(10)	-1.41740(6)	-1.59608
1.86[a]	20000	65.16(13)	-1.38638(9)	-1.7856
1.86[a]	40000	112.98(18)	-1.29844(18)	-2.2149
1.86[a]	60000	167.7(2)	-1.1854(2)	-2.69739
1.86[a]	80000	229.42(15)	-1.04980(12)	-3.22147
1.86[c]	125000	378(2)	-0.743(3)	-4.51072
1.86[b]	250000	918.6(1.3)	0.2491(18)	-8.65932
1.86[b]	333333	1340.7(1.3)	0.9607(18)	-11.7193
1.86[b]	500000	2214.5(1.7)	2.336(2)	-18.3468
1.86[b]	571428	2595(2)	2.910(3)	-21.3458
1.86[b]	666667	3104(3)	3.661(4)	-25.4472
1.86[b]	800000	3818(3)	4.699(4)	-31.3521
1.86[b]	1×10^6	4876.7(1.5)	6.212(2)	-40.5306
1.86[b]	2×10^6	10128(3)	13.559(3)	-90.3193
1.86[b]	4×10^6	20550(5)	27.959(7)	-199.554
1.86[b]	8×10^6	41316(7)	56.543(9)	-437.845
1.86[d]	16×10^6	82822	113.69	-955.409
1.86[d]	32×10^6	165822	227.79	-2068.45
1.86[d]	64×10^6	331768	455.87	-4450.87
1.86[d]	128×10^6	663625	911.93	-9537.1
1.86[d]	256×10^6	1327312	1824.01	-20338.8
1.86[d]	512×10^6	2654668	3648.12	-43196.4
1.86[d]	1024×10^6	5309366	7296.30	-91478.5
1.86[d]	2048×10^6	10618754	14592.66	-193062
1.75[a]	1000	22.14(4)	-1.443419(13)	-1.45302
1.75[a]	3000	32.35(11)	-1.43604(4)	-1.47673
1.75[a]	5000	40.66(13)	-1.42933(5)	-1.50576
1.75[a]	10000	57.60(13)	-1.41415(6)	-1.58867
1.75[a]	20000	87.06(17)	-1.38263(11)	-1.77422
1.75[a]	40000	144.6(3)	-1.2961(3)	-2.19531
1.75[a]	60000	210.43(19)	-1.18602(16)	-2.66885
1.75[a]	80000	284.6(3)	-1.05398(16)	-3.18308
1.75[b]	125000	454.4(1.0)	-0.7647(12)	-4.44653
1.75[b]	250000	1098.0(1.1)	0.2015(13)	-8.50508
1.75[b]	500000	2639.1(1.6)	2.2626(17)	-17.9781
1.75[b]	1×10^6	5831.7(2.0)	6.143(2)	-39.7109
1.75[b]	2×10^6	12139(2)	13.503(3)	-88.6228
1.75[b]	4×10^6	24656(3)	27.915(4)	-196.115
1.75[b]	8×10^6	49587(8)	56.501(10)	-430.926
1.75[d]	16×10^6	99420	113.65	-941.531
1.75[d]	32×10^6	199083	227.76	-2040.64
1.75[d]	64×10^6	398335	455.85	-4395.24
1.75[d]	128×10^6	796789	911.92	-9425.79
1.75[d]	256×10^6	1593662	1824.00	-20115.4
1.75[d]	512×10^6	3187384	3648.11	-42749
1.75[d]	1024×10^6	6374809	7296.30	-90584.7
1.75[d]	2048×10^6	12749648	14592.65	-191274

This approach smoothly connects the low- and high-temperature limits. When we refer to excess pressures and internal energies below we mean the difference to this ideal chemical model. For the correct interpretation of the presented graphs, it should be pointed out that the pressures and energies of the ideal model depend on the Saha ionization equilibrium. If the ideal system exhibits a higher degree of ionization than the simulation results, then this alone can lead to negative excess pressures and energies, which one would normally attribute exclusively to the interaction of free electrons and ions. This fact is relevant for the correct interpretation of Fig. 3 where even the DFT-MD results without thermally excited electrons exhibit a negative excess internal energy at 80 000 K.

TABLE IV: Table III continued.

r_s	T(K)	P (GPa)	E/N_e (Ha)	F/N_e (Ha)
1.5[a]	1000	73.92(10)	-1.43440(3)	-1.44135
1.5[a]	2000	84.42(12)	-1.42977(4)	-1.45018
1.5[a]	3000	92.66(12)	-1.42576(4)	-1.46128
1.5[a]	5000	107.7(2)	-1.41813(7)	-1.48725
1.5[a]	10000	137.9(3)	-1.40115(11)	-1.56358
1.5[a]	20000	189.4(4)	-1.36731(18)	-1.73814
1.5[a]	40000	285.0(4)	-1.2819(2)	-2.13878
1.5[a]	60000	387.4(4)	-1.1802(2)	-2.58963
1.5[a]	80000	505.3(3)	-1.05690(13)	-3.07884
1.5[b]	125000	770(2)	-0.7880(16)	-4.27821
1.5[b]	250000	1737.1(1.6)	0.0907(12)	-8.11696
1.5[b]	500000	4114.7(1.6)	2.0709(12)	-17.0558
1.5[b]	1×10^6	9147.6(1.6)	5.9425(12)	-37.6523
1.5[b]	2×10^6	19175(2)	13.3390(15)	-84.3488
1.5[b]	4×10^6	39062(5)	27.782(4)	-187.433
1.5[b]	8×10^6	78690(10)	56.411(8)	-413.442
1.5[c]	16×10^6	157860(7)	113.544(5)	-906.451
1.5[d]	32×10^6	316058	227.68	-1970.31
1.5[d]	64×10^6	632486	455.79	-4254.46
1.5[d]	128×10^6	1265232	911.88	-9143.99
1.5[d]	256×10^6	2530649	1823.97	-19550.3
1.5[d]	512×10^6	5061428	3648.09	-41618.1
1.5[d]	1024×10^6	10122947	7296.28	-88324.9
1.5[d]	2048×10^6	20245959	14592.64	-186751
1.25[a]	3000	331.6(3)	-1.39652(6)	-1.42554
1.25[a]	5000	360.1(5)	-1.38761(12)	-1.44742
1.25[a]	10000	418.6(4)	-1.36798(8)	-1.51449
1.25[a]	20000	515.4(8)	-1.3306(3)	-1.67468
1.25[a]	40000	683.9(5)	-1.24615(18)	-2.05136
1.25[a]	60000	865.2(7)	-1.1504(2)	-2.47506
1.25[a]	80000	1063.2(1.0)	-1.0378(3)	-2.93438
1.25[a]	125000	1565.4(1.5)	-0.7817(4)	-4.05965
1.25[b]	250000	3074(3)	-0.0069(11)	-7.65192
1.25[b]	500000	6999(4)	1.8502(15)	-15.9783
1.25[b]	1×10^6	15578(3)	5.6796(11)	-35.2469
1.25[b]	2×10^6	32897(7)	13.107(3)	-79.3259
1.25[b]	4×10^6	67243(80)	27.58(3)	-177.186
1.25[b]	8×10^6	135808(19)	56.263(8)	-392.772
1.25[b]	16×10^6	272614(30)	113.381(13)	-864.979
1.25[d]	32×10^6	545908	227.54	-1887.16
1.25[d]	64×10^6	1092767	455.69	-4087.74
1.25[d]	128×10^6	2186203	911.81	-8810.14
1.25[d]	256×10^6	4372877	1823.92	-18883.5
1.25[d]	512×10^6	8746088	3648.06	-40286
1.25[d]	1024×10^6	17492411	7296.26	-85659.8
1.25[d]	2048×10^6	34984988	14592.63	-181419

TABLE V: Table IV continued.

r_s	T(K)	P (GPa)	E/N_e (Ha)	F/N_e (Ha)
1[a]	5000	1560.1(5)	-1.29739(8)	-1.34504
1[a]	10000	1681.8(7)	-1.27401(12)	-1.40096
1[a]	20000	1878.6(1.0)	-1.2313(2)	-1.5439
1[a]	40000	2217.0(1.8)	-1.1449(3)	-1.88916
1[a]	62500	2608.7(1.8)	-1.0456(3)	-2.33028
1[a]	80000	2941(2)	-0.9554(4)	-2.7022
1[a]	125000	3890(2)	-0.7276(4)	-3.73996
1[b]	250000	6640(6)	-0.0380(12)	-7.04803
1[b]	333333	8780(6)	0.4717(12)	-9.46272
1[b]	500000	13687(5)	1.6229(11)	-14.6687
1[b]	571428	15920(5)	2.1410(11)	-17.0286
1[b]	666667	18969(5)	2.8429(11)	-20.2721
1[b]	800000	23334(5)	3.8385(12)	-24.9776
1[b]	1×10^6	29972(5)	5.3367(12)	-32.3609
1[b]	2×10^6	63676(11)	12.775(2)	-73.2177
1[b]	4×10^6	130941(12)	27.326(3)	-164.669
1[b]	8×10^6	264847(50)	56.052(10)	-367.49
1[c]	16×10^6	532209(20)	113.270(5)	-814.18
1[c]	32×10^6	1066140(60)	227.350(14)	-1785.39
1[d]	64×10^6	2133644	455.50	-3884.05
1[d]	128×10^6	4269457	911.68	-8402.62
1[d]	256×10^6	8540444	1823.83	-18068.8
1[d]	512×10^6	17081968	3647.99	-38656.7
1[d]	1024×10^6	34164699	7296.21	-82400.7
1[d]	2048×10^6	68329938	14592.59	-174902

Figure 3 exhibits the missing correlation energy in DFT GGA, which underestimates the binding energy of the atom by ΔE_0= 36 mHa compared to the exact non-relativistic goundstate energy of $-2.9037\,\mathrm{Ha}$[49–51]. This is the main reason for the deviation of 22 mHa per electron from the ideal plasma model at 1000K. The ideal plasma model that was constructed using the exact groundstate energy. The remainder of the discrepancy, 4 mHa per electron, is due to the change in the internal energy associated to the compression to a density of $r_s = 1.86$ and to the fact that the comparison is made for 1000K.

To correct for missing correlation energy, we applied a uniform correction of $-\Delta E_0$ to all DFT results discussed later. We may assume that the correction to DFT depends only weakly on temperature and density. Determining its precise amount more accurately is difficult and goes beyond the scope of this article.

Despite this DFT insufficiency, one finds reasonably good agreement in the internal energies reported by PIMC and DFT-MD. Figure 3 shows that both methods report very similar increases in the energy resulting from thermal population of unoccupied electronic states, which is the basis for constructing one EOS table.

In order to explore the agreement between PIMC and DFT-MD in more detail, we resort to pressure calculations for a single configuration of nuclei that we have obtained from DFT-MD with 57 atoms at 80 000 K. The nuclear coordinates of the $r_s = 1.86$ snapshot are given in Tab. A in the appendix. For this fixed configuration of nuclei, we now compare the instantaneous pressure as a function of electronic temperature. The fact that the nuclei are now classical rather being represented by paths in PIMC has a negligible effect on the pressure for the temperatures under consideration. In both methods, the instantaneous pressure is a well-defined quantity derived from the virial theorem. In PIMC, the pressure is derived directly from the kinetic, $\langle\mathcal{K}\rangle$, and potential, $\langle\mathcal{V}\rangle$, energy,

$$3PV = 2\langle\mathcal{K}\rangle + \langle\mathcal{V}\rangle \ , \tag{5}$$

where V is the volume of the simulation cell. In DFT, one

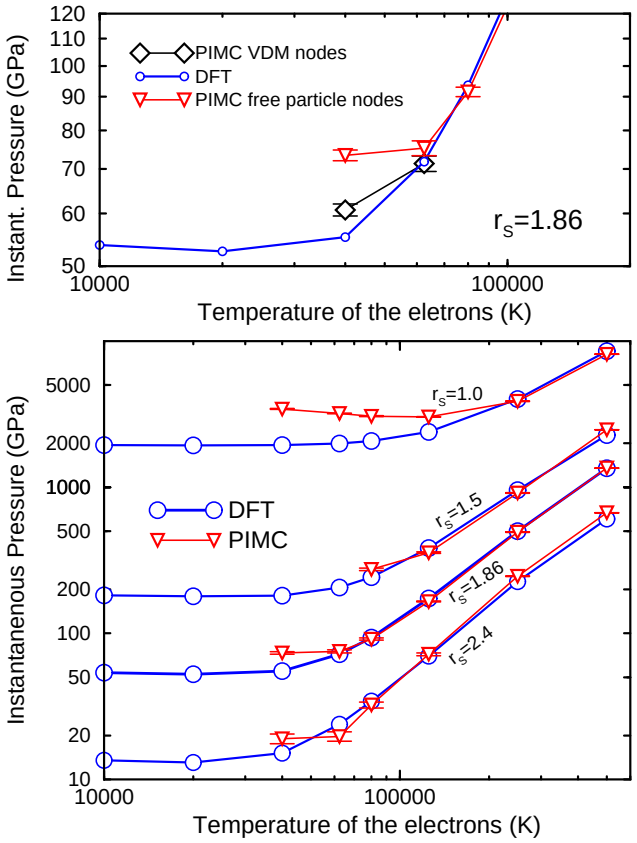

FIG. 4: Comparison of the instantaneous pressure for a fixed configuration of nuclei derived from PIMC and DFT with thermally populated states. The upper panel included results from PIMC with variational nodes. The lower panel compares PIMC results with free-particle nodes for different densities. (The ideal gas contributions from the nuclei are not included.)

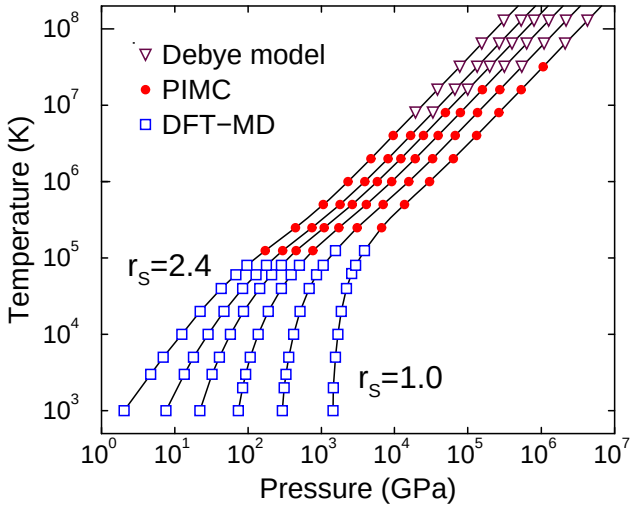

FIG. 5: Pressure-temperature diagram that indicates the conditions where PIMC (circles) and DFT-MD (squares) simulations have been performed. The lines show isochores for the following r_s parameters: 2.4, 2.0, 1.75, 1.5, 1.25, and 1.0. The triangles indicate conditions where the Debye model has been used.

uses the diagonal elements of the stress tensor[52]. For a fixed configuration of nuclei, the temperature dependence of the instantaneous pressure arise from changes in the thermal population of Kohn-Sham orbitals.

Figure 4 compares the instantaneous pressures from both methods. At intermediate temperatures, there is a large interval where both methods agree. DFT pressures appear to be fairly accurate. For the level of accuracy needed for this study we could not detect any insufficiency resulting from the groundstate exchange correlation functional nor from inaccurate thermal excitations resulting from an underestimated band gap. However, the DFT eventually becomes prohibitively expensive at higher temperature. Some of the points at $r_s = 2.4$ required up to 100 bands per atom, and that is one reason why we only used a single configuration. The other comes from path integrals. PIMC simulations with 123 atoms, shown in Fig. 1, represent about the limit one can study with currently available computers. To repeat the calculations at lower temperature where the paths are longer, or to use the more expensive variational nodes, would quickly exceed existing limits in processing power.

Figure 4 also reveals inaccuracies in the PIMC computation that are caused by approximations in the trial density matrix. PIMC with free-particle nodes predict pressures that are too high when the electrons settle into the ground state ($T \leq 40\,000$ K for r_s=1.86 as shown in Fig. 2). This effect has already been reported for hydrogen[15]. In the variational density matrix approach[37] one allows the trial density matrix to adjust to the positions of the nuclei, which corrects most of the pressure error as can be seen in upper panel of Fig. 4. However, the variational approach was derived to study finite temperature problems. It does not describe the electronic ground state as well as DFT.

For the purpose of constructing one EOS table for helium, we use our DFT-MD results with $T_{\rm el} = T_{\rm ion}$ up to 80 000 K for $r_s \geq 1.5$ and results up to 125 000 K for $r_s = 1.25$ and 1.0. For all higher T, we use PIMC simulations, which become increasingly efficient at higher T because the length of the paths is inversely proportional to temperature. The temperature-pressure conditions of DFT-MD and PIMC simulations are shown in Fig. 5.

It should noted that the discussed validity range of different trial density matrices depends very much on the material under consideration. The temperature where we switch from PIMC to DFT-MD reflects the degree of thermal electronic excitations as well as some dependence of the approximations made in each methods. The density dependence of the switching temperature would typically be estimated by comparing the temperature to the Fermi energy of an ideal gas of electrons. However, to incorporate band structure effects of dense helium, we found it more appropriate to relate the switching temperature to the DFT band width. Band width and Fermi

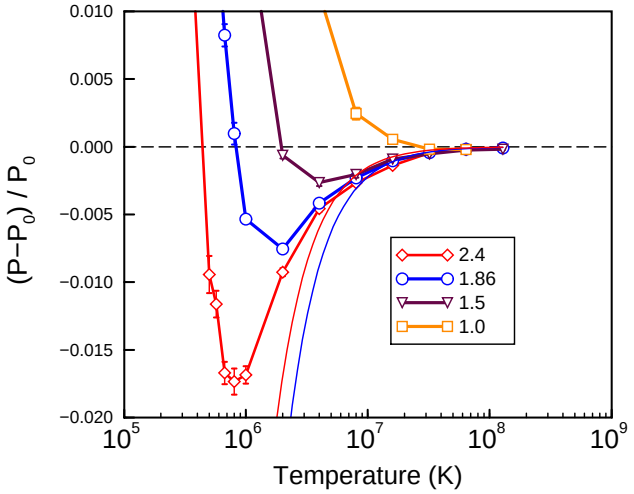

FIG. 6: The relative excess pressure derived from PIMC (thick lines with symbols) is compared with Debye-Hückel plasma model (thin lines) for different values of r_s given in the legend. The ideal pressure, P_0, is derived Saha model of noninteracting helium species (see text).

energy are identical in systems of noninteracting particles. For the purpose of this study, we found it appropriate to switch from PIMC to DFT-MD for temperatures corresponding to less than one third of the helium band width.

We performed PIMC simulations up to 1.28×10^8 K covering a large temperature interval of two orders of magnitude. At low temperature, the excess internal energies and pressures in Figs. 2, 3, and 6 are positive because of thermal electronic excitations, but then change sign due to interactions of ions and free electrons. At very high temperature when helium is fully ionized, the system can be described by the Debye plasma model[53]. The Debye model is based on a self-consistent solution of the Poisson equation for a system of screened charges. The excess contribution to the free energy, internal energy, entropy per particle, and pressure are given by,

$$\frac{F}{N_\mathrm{p}} = \frac{\Xi}{12} \;,\quad \frac{E}{N_\mathrm{p}} = \frac{\Xi}{8} \;,\quad \frac{S}{N_\mathrm{p}} = \frac{\Xi}{24} \;,\quad P = \frac{\Xi}{24V} \;, \tag{6}$$

$$\Xi = -k_B T V \frac{\kappa^3}{\pi} \quad , \quad \kappa^2 = \frac{4\pi}{k_B T} \sum_i Z_i^2 \frac{N_i}{V}, \tag{7}$$

where $\kappa = 1/r_d$ is the inverse of Debye radius, r_d, in a collection of N_i particles of charge Z_i in volume V where $N_\mathrm{p} = \sum_i N_i$. Figure 6 demonstrate very good agreement with the Debye model at high temperature. The Debye model fails at lower temperatures where it predicts unphysically low pressures. Under these conditions the screening approximation fails because there are too few particles in the Debye sphere. The number of particles in the Debye sphere is proportional to,

$$(r_d/r_s)^3 \sim (T\, r_s)^{3/2} \;, \tag{8}$$

which means that the Debye model becomes increasingly accurate for high T and large r_s. This is exactly what is observed in Fig. 6. For higher densities, PIMC and Debye predictions converge only at higher temperatures.

The size of the Debye sphere increases with temperature and will eventually exceed the size of any simulation cell. This occurs when the coupling of the particles becomes very weak. With increasing temperature, the Coulomb energy decreases while the kinetic energy increases linearly with T. Determining the precise amount of the Coulomb energy becomes increasingly difficult due to finite size effects. The finite size extrapolation only corrects for the leading term in an expansion in $1/N$. In the weak coupling limit, bigger and bigger simulation cells are needed to perform the extrapolation accurately. Instead of using simulations, it is much more efficient to switch to analytical methods like the hypernetted chain integral equations[54] or the Debye model.

In conclusion, finite size effects are the reason why the PIMC energies do not agree perfectly with the Debye model for the highest temperature shown in the lower panel of Fig. 3. The excess pressures reported in Fig. 6 are less sensitive to finite size errors than the internal energy because their volume dependence is relatively weak. We consequently use the Debye EOS for the highest temperatures in our EOS given in Tab. I. The pressure-temperature conditions for DFT-MD, PIMC, and Debye results are summarized in Fig. 5.

IV. COMPARISON WITH FREE ENERGY MODELS

Now we compare our first-principles EOS with chemical free energy models that were developed before first-principles simulation data became available. Winisdoerffer and Chabrier[55] constructed a semianalytical model to study stellar interiors that covers a wide density range including metallization. Their EOS is only available in explicit form in a small temperature interval, and a comparison with DFT-MD simulation has already been reported[22]. That is why we focus on three other free energy models: the first derived by Saumon, Chabrier, and van Horn (SCvH)[56], another by Chen *et al.*[57], and one model by Förster, Kahlbaum and Ebeling[58].

The SCvH EOS for helium combined with their hydrogen EOS[59] has been used numerous times to model giant planet interiors. Figure 7 compares the excess pressure for three different temperatures. At a high temperature of 10^6K, which is important for stellar interiors, we found fairly good agreement. The deviations between the SCvH model and PIMC simulations are only about 4%.

At a intermediate temperature of 100 000 K, which approximately represents the regime of shock wave experiments, the agreement is less favorable. The SCvH EOS reports pressures that are about 30% lower than those predicted by PIMC. This is partly due to the fact that the SCvH model follows the Debye model down to too

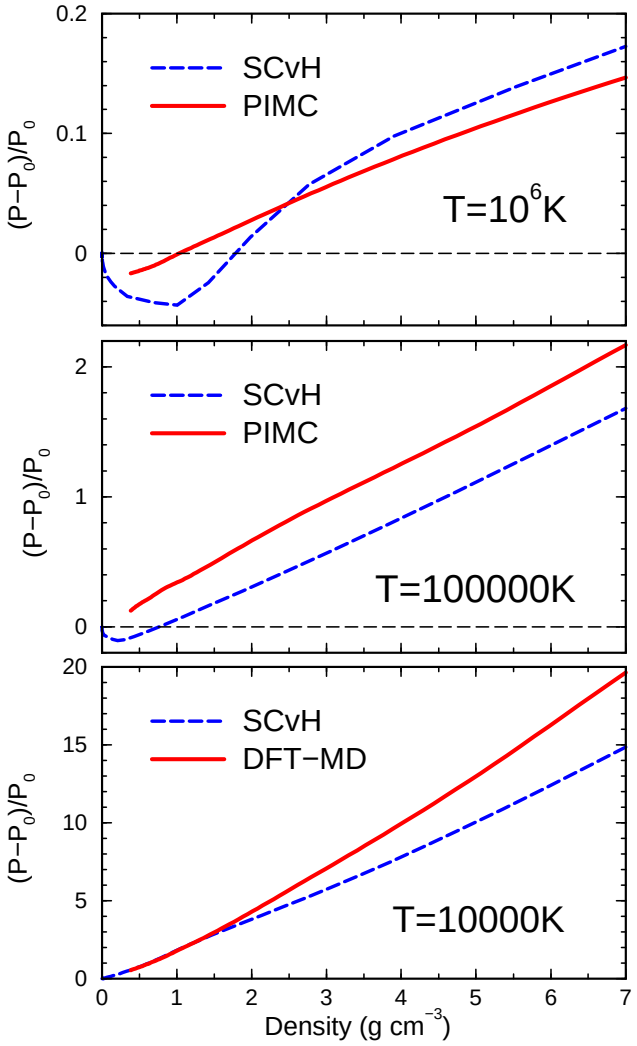

FIG. 7: Comparison of the relative excess pressure reported by first-principles simulations with the SCvH EOS model. The three temperatures shown here are relevant for stellar interiors, the comparison with shock wave experiments, and the interiors of giant planets.

low temperatures (Fig. 3). Furthermore, the authors of the SCvH EOS relied on an interpolation scheme between low and high temperature expressions to construct their helium EOS. At intermediate temperatures the resulting EOS is not thermodynamically consistent. The authors reported the region of inconsistency in their article[56] and we added it to Fig. 17.

The last panel in Fig. 7 is relevant to the interiors of giant planets with temperature of order 10 000 K. At low density both EOSs agree well, but above 1.5 g cm^{-3} deviation begin to increase steadily. At conditions comparable to Jupiter's interior, we find that the SCvH underestimates the pressure by 30%. In a hydrogen-helium mixture of solar composition, this translates into an error in the pressure of about 4%. This is the reason why even the helium EOS is important for estimating the size

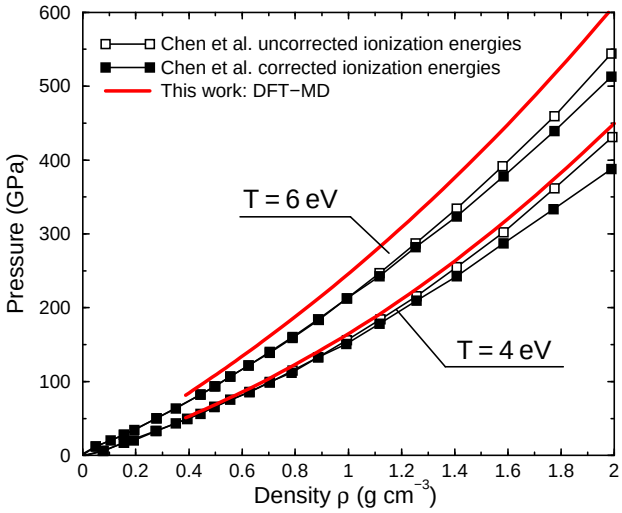

FIG. 8: EOS comparison with the free energy model by Chen et al.[57] for two temperatures of 4 and 6 eV.

of Jupiter's core, which is expected to be only a small fraction of Jupiter's total mass[25,26,60].

Figure 8 compare the pressures with the free energy model derived by Chen *et al.*[57]. For the conditions of $\rho < 2$ g cm^{-3} and 4 eV $< T <$ 6 eV, the agreement with the first-principles EOS reported here is reasonably good. The deviations are of order 10%. However, one motivation of the Chen *et al.* work was the consideration of a density and temperature dependent correction to the ionization energy. Figure 8 shows that the deviation from the first-principles EOS increases when this correction is applied. Since the assumption of a lowering of the ionization energy with density is very reasonable, one expects the reason for the discrepancy to be caused by one of the many other approximations in this chemical model.

In 1992, Förster, Kahlbaum, and Ebeling (FKE) derived a chemical model for dense helium that exhibits two first-order phase transitions associated with the ionization steps He $\rightarrow$ He$^+$ $\rightarrow$ He^{2+} at high density and low temperature. The authors were careful to point out that there is no final proof for the existence of such plasma phase transitions in helium but constructed their model so that possible consequences in astrophysics could be explored. Figure 9 compares the FKE model with the first-principles EOS reported here. Both phase transitions were predicted to occur in a temperature and density region where the first-principles EOS is perfectly smooth and no evidence of a sharp ionization transition can be found. Good agreement with the FKE EOS is observed for low density and high temperature where chemical models work well. Also at very high density outside the region of the predicted phase transitions, the agreement is very reasonable.

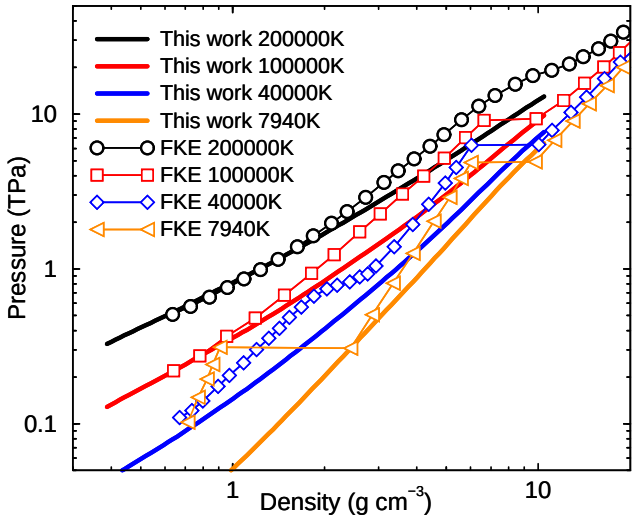

FIG. 9: EOS comparison with the free energy model by Förster, Kahlbaum, and Ebeling[58] (FKE) that exhibits two first-order phase transitions.

V. PAIR CORRELATION FUNCTIONS

In this section, we study the structure of the fluid by analyzing correlations between different types of particles. Given the large amount of simulation results, we focus our attention primarily on the temperature dependence and only report results for one density of $r_s = 1.86$. The density dependence of the pair correlation functions, $g(r)$, has been analyzed in Ref.[48] for hydrogen and in Ref.[61] for helium.

Figure 10 shows how the nuclear pair correlation functions changes over a temperature interval that spans seven orders of magnitude. At low temperature, the $g(r)$ shows the oscillatory behavior that is typical for a hard-sphere fluid. The atomic interactions are governed by two tightly bound electrons that lead to a strong repulsion at close range due to Pauli exclusion. As long as the density is not too high, this behavior is well-described by the Aziz pair potential[20].

As temperature increases, two effects change the pair correlation function. First, the increase in kinetic energy leads to stronger collisions, and atoms approach each other more. In this regard, helium does not exactly represent a hard-sphere fluid because the Aziz pair potential is not perfectly hard. Second, the increase in temperature also damps of the oscillation in the $g(r)$.

At 80 000 K, one finds perfect agreement between PIMC and DFT-MD (upper panel in Fig. 10). As the temperature is increased further, changes in the nuclear $g(r)$ functions are dominated by thermal electronic excitations and the ionization of atoms. One finds that the strong repulsion at low temperature disappears gradually. As the Debye-Hückel limit is approached, the fluid behaves like a correlated system of screened Coulomb charges.

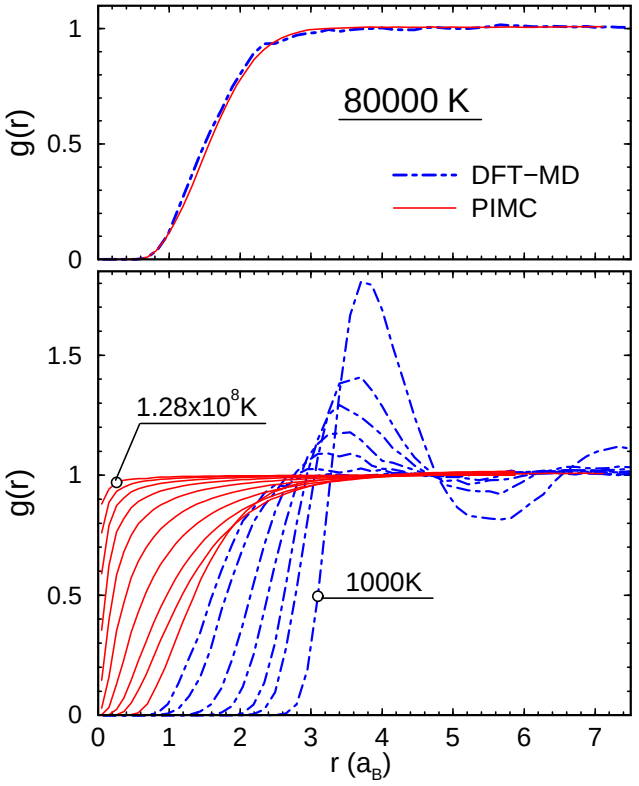

FIG. 10: The nuclear pair correlation functions for $r_s = 1.86$. The lower panel shows the following temperatures: { 128, 64, 32, 16, 8, 4, 2, 1, 0.5, and 0.125 } $\times 10^6$ K from PIMC as well as { 40, 20, 10, 5, 3, and 1 } $\times 10^3$ K from DFT-MD.

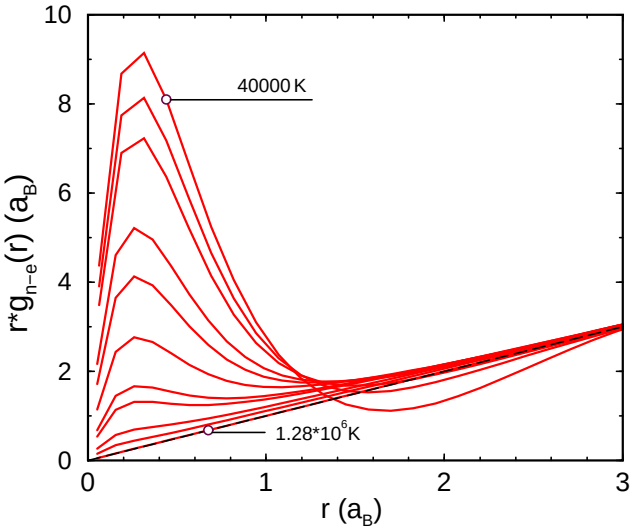

FIG. 11: The electron-nucleus pair correlation functions, $g(r)$, from PIMC for $r_s = 1.86$. Starting with the highest peak, the following temperatures are plotted: { 0.04, 0.08, 0.125, 0.25, 0.333, 0.5, 0.8, 1, 2, 4, and 128 } $\times 10^6$ K. We plot $r * g(r)$ on the ordinate so that the peak at small r illustrates the fraction of electrons in bound states. The decrease in peak height with increasing temperature demonstrates thermal excitation of electrons, which eventually leads the ionization of atoms.

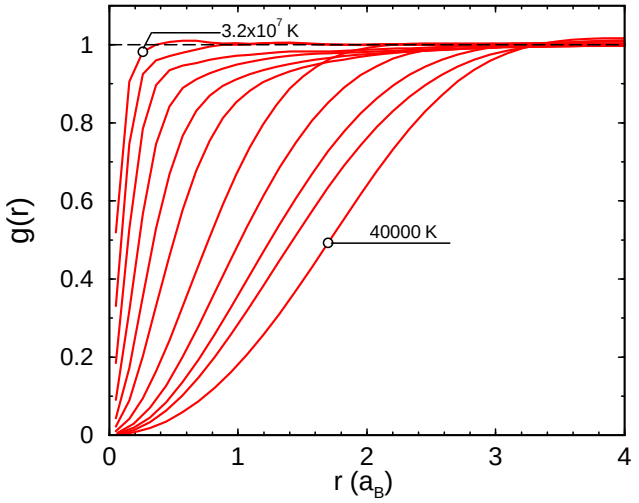

FIG. 12: The electron-electron pair correlation functions for electrons with parallel spins calculated with PIMC for $r_s = 1.86$. Starting from the left, the following temperatures are plotted: { 32, 16, 8, 4, 2, 1, 0.25, 0.125, 0.08, 0.0625, 0.04 } $\times 10^6$ K. With increasing temperature, correlation effects are reduced and the exchange-correlation hole disappears.

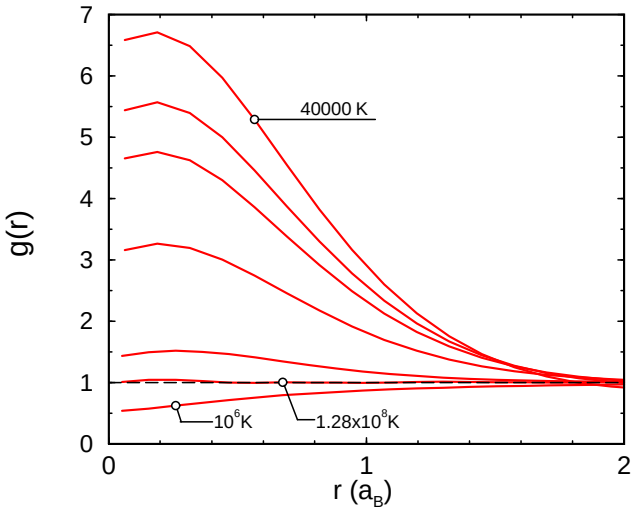

FIG. 13: The electron-electron pair correlation functions for electrons with opposite spins calculated with PIMC for $r_s = 1.86$. Starting from the top, the following temperatures are plotted: { 0.04, 0.0625, 0.08, 0.125, 128, and 1 } $\times 10^6$ K. The smallest values are observed for 10^6 K.

The peak in the electron-nucleus pair correlation functions in Fig. 11 illustrates that the electrons are bound to the nuclei. At 40 000 K and below, the peak height is maximal. At higher temperature, electrons get excited thermally and eventually atoms become ionized. The peak height is consequently reduced until, at very high temperature, the motion of electrons and nuclei becomes uncorrelated.

The correlation of electrons with parallel spins is determined by Pauli exclusion and Coulomb repulsion but is also influenced by the motion of the nuclei at low temperature. Combination of all these effects causes the motion of same-spin electrons to be negatively correlated at small distances. This is typically referred to as the exchange-correlation hole. At high temperatures, kinetic effects reduce the size of this hole but $g(r)$ always goes to zero for small r due to Pauli exclusion.

Despite the Coulomb repulsion, the electrons with opposite spins are positively correlated at low temperature, because two electrons with opposite spin are bound in a helium atom. With increasing temperature, the peak in Fig. 13 reduces in height because more and more electrons get ionized. At 10^6 K, one finds the lowest values for $g(r \to 0)$ because the electrons are anti-correlated due to the Coulomb repulsion. If the temperature is increased further, kinetic effects dominate over the Coulomb repulsion and $g(r \to 0)$ again increases and will eventually approaches 1 at high temperature.

VI. ELECTRONIC DENSITY OF STATES

In this section, we illustrate the importance of thermal electronic excitation by analyzing the electronic density of states (DOS) derived from DFT-MD[22,24]. Figure 14 compares the total available DOS as well as the thermally occupied fraction for $r_s = 1.0$, 1.86, and 2.2 and T=80 000 , 20 000, and 5 000 K. The results were obtained by averaging over 10 snapshots equally spaced from corresponding DFT-MD trajectories. The eigenvalues of each snapshot were shifted so that the Fermi energies align at zero. A 4x4x4 k-point grid was used for $r_s = 1.0$ and 1.86, and a 2x2x2 grid for r_s=2.2. To reduce the remaining noise level, a Gaussian smearing of 1 eV was applied to the $r_s = 2.2$ and 1.86 results; 2 eV was used for r_s=1.0. The curves are normalized such that the occupied DOS integrates to 1.

The electronic DOS at $r_s = 2.2$ and 1.86 are qualitatively similar. The occupied DOS has one large peak at approximately −10 eV, followed by a wide gap at the Fermi energy, followed by a continuous spectrum of conducting states. At 5000 K, thermal electronic excitations are not important. At 20 000 K, a small but non-negligible fraction of the electrons are excited across the gap, which is illustrated in the inset in the middle panel of Fig. 14. These excitations increase the pressure shown in Fig. 2 and increase the compression ratio in shock wave experiments that will be discussed later. At 80 000 K the system still exhibits a gap but a large fraction of the electrons now occupy excited states. The increase in temperature also lead to stronger collisions of the atoms, which broadens the peak of the unoccupied DOS and spreads the levels in the unoccupied DOS further, which

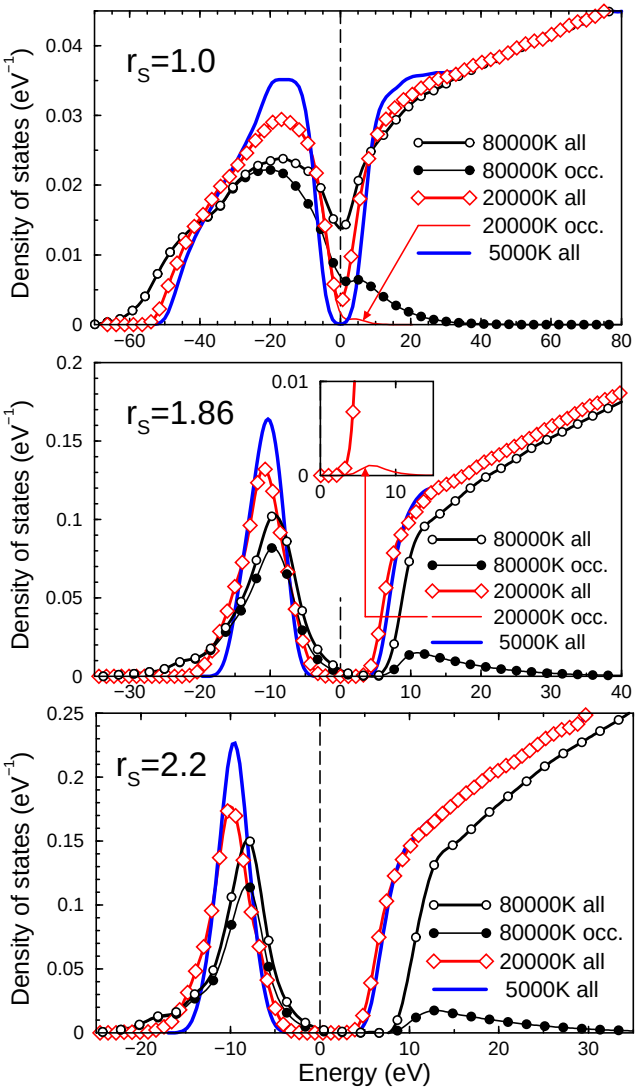

FIG. 14: The three panels show the electronic density of states (DOS) at the densities r_s = 1.0, 1.86, and 2.2. The open and filled circles, respectively, show th density of all available states and the thermally occupied fraction at 80 000 K. The diamonds and the thick lines without symbols show total DOS at 20 000 and 5 000 K, respectively. The occupied DOS at 20 000 K (this solid line) is only shown for $r_s = 1.0$ and in the inset for $r_s = 1.86$. The eigenvalues from each configuration were shifted so that all Fermi energies (vertical dashed line) align at zero.

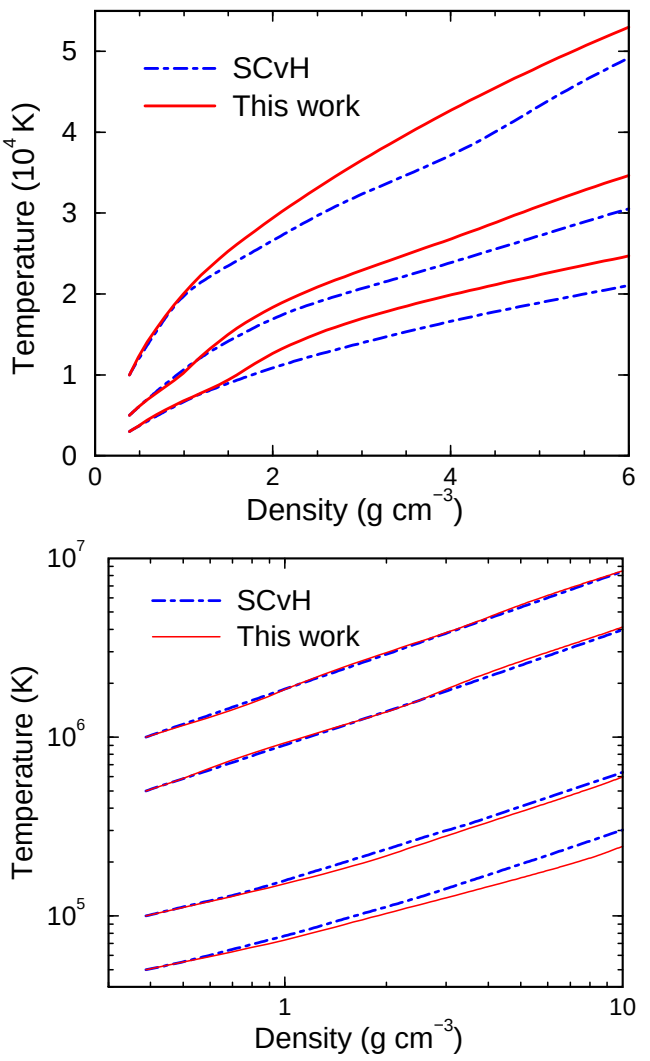

FIG. 15: Comparison in temperature-density space of adiabats from first-principles simulations (this work) and the SCvH EOS model.

reduces the magnitude DOS.

At r_s=1.0 the character of the DOS is different from lower densities. At 5000 K, the system still exhibits a gap, but it is much narrower. Occupied and unoccupied states are piled up around it. The band width of the occupied states has increased substantially[24]. If temperature is increased at this density, the band gap closes as a result of the collision induced broadening. Fluid helium assumes a metallic state that has been studied in more detail in Refs.[22,24].

VII. ENTROPY CALCULATIONS

Convection in the interior of planets requires that the temperature-pressure profile is adiabatic. In consequence, the planetary interior is fully determined by the conditions on the surface and the EOS. This makes the calculation of adiabats important. However, neither Monte Carlo nor molecular dynamics methods can directly compute entropies because both techniques save orders of magnitude in computer time by generating only a representative sample of configurations. Without this gain in efficiency, many-body simulations would be impossible. In consequence, entropies that are measures of the total available phase space are not accessible directly.

Typically one derives the entropy by thermodynamic integration from a know reference state. However, for planetary interiors, the absolute value of the entropy is not important as long as one is able to construct (T, P)

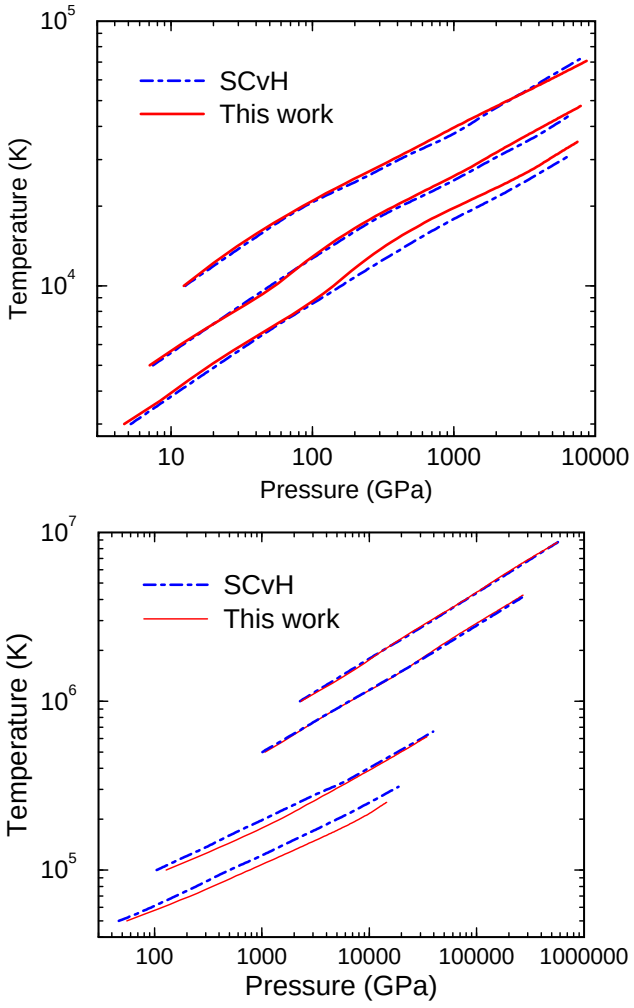

FIG. 16: Comparison in temperature-pressure space of the adiabats shown in Fig. 15.

curves of constant entropy. This can be done using the pressure and the internal energy from first-principles simulations at different (T, V) conditions. Using Maxwell's relations, one finds,

$$\left.\frac{\partial T}{\partial V}\right|_S = -\frac{\left.\frac{\partial S}{\partial V}\right|_T}{\left.\frac{\partial S}{\partial T}\right|_V} = -T\frac{\left.\frac{\partial P}{\partial T}\right|_V}{\left.\frac{\partial E}{\partial T}\right|_V} \,. \qquad (9)$$

By solving this ordinary differential equation, (V,T)-adiabats can be constructed as along as a sufficiently dense mesh of high-quality EOS points are available to make the required interpolation and differentiation of E and P with respect to temperature satisfactorily accurate.

One drawback of formula (9) is that it is not necessarily thermodynamically consistent if pressures and internal energies are interpolated separately. This is the primary reason why we developed the following method to fit the free energy instead. Pressure and internal energy are related to the free energy, $F(V,T)$, by

$$P = -\left.\frac{\partial F}{\partial V}\right|_T \quad \text{and} \quad E = F - T\left.\frac{\partial F}{\partial T}\right|_V \,. \qquad (10)$$

Different EOS fits for fluids have been proposed in the literature[47,62]. Thermodynamic consistency was not a priority in either case. Both papers relied on specific functional forms that were carefully adjusted to the material under consideration. Although such a fit of specific form could probably have also been constructed for the presented helium EOS data, we wanted to have an approach that is not just applicable to one material. Therefore, we decided to represent the free energy as a bi-cubic spline function with temperature and density as parameters. This spline function can accurately represent our helium EOS data and can easily be adapted to fit other materials. Cubic splines are twice continuously differentiable, which means the derived pressures and energies are once continuously differentiable with respect to V and T. This is sufficient for this study. If additional thermodynamic functions that require higher order derivatives of the free energy, such as sound speeds, need to be fit also, then higher order splines can accommodate that.

We start the free energy interpolation by constructing a series of one-dimensional spline functions $F_n(T)$ for different densities. The choice of knots T_i is arbitrary. Their location should be correlated with the complexity of the EOS as well as the distribution of EOS data points. In our helium example, we used a logarithmic grid in temperature with about half as many knots as data points. The set of free energy values on the knots, $F(T_i)$, represent the majority of the set of fit parameters. In addition, one may also include the first derivatives of the splines $\frac{\partial F_n}{\partial T}|_V$ at the lowest and highest temperatures, which represent the entropy. Alternatively, one could derive those derivatives by other means and then keep them fixed during the fitting procedure.

To compute the free energy at a specific density, n^*, and temperature, T^*, we first evaluate all splines $F_n(T^*)$ and then construct a secondary spline at constant temperature as a function of density, $F_{T^*}(n)$. Its first derivate is related to the pressure. Again, the derivative at the interval boundaries can either be fixed or adjusted during the fitting procedure. We adjust them by introducing an additional spline $\frac{\partial F}{\partial n}|_T(T)$ at the lowest and highest densities, which then get adjusted in the fitting procedure.

We begin the fitting procedure with an initial guess for the free energy function derived from Eq. (9). Then we employ conjugate gradient methods[63] to optimize the whole set of fitting parameters. Minimizing the sum of the squared relative deviations in pressure and internal energy has been found to work best. (Just for the derivation of the relative deviation in energy, the zero of energy has been shifted to the value of the isolated helium atom.)

All fits tend to introduce wiggles if too many free parameters are included. We control wiggles by adjusting the number of knots in density and temperature but we

also introduce penalty in the form,

$$\xi = \int d\rho \left(\frac{\partial^3 F}{\partial n^3} \right)^2 \quad , \tag{11}$$

to favor fits with smaller $|\partial^2 P/\partial n^2|$. Finally we change the density argument in the spline interpolation from $F_T(\rho)$ to $F_T(\log(\rho))$. This improves the fit in the high temperature limit where the free energy is dominated by the ideal gas term that has logarithmic dependence on density.

The presented free energy fit is thermodynamically consistent by construction. It allows us to accurately represent the entire data set of P and E values. Without additional information, the free energy can be determined up to a term $T\Delta S$, which is sufficient to compute adiabats. To determine the absolute value of the entropy, one needs an anchor point, for which the entropy was derived by different means.

Figure 15 compares different adiabats derived from our first-principles EOS with predictions from the SCvH EOS model. Beginning from a joint starting point of $r_s = 2.4$ and a selection of seven different temperatures of 3000, 5000, 10 000, 50 000, 100 000, 500 000, and 10^6 K, we constructed the adiabats for both models for the density interval under consideration. The upper panel of Fig. 15 demonstrates good agreement between both methods at low densities up to about 1 g cm^{-3}. For higher densities, one finds deviations of up to 20% in the predicted temperatures on the adiabats. A higher temperature, the agreement get substantially better, which is illustrated in the lower panel of Fig. 15. The observed deviations are similar to pressure differences shown in Fig. 7.

For applications in the field of planetary science, we also show the adiabats in (T,P) space in Fig. 16. The deviations are comparable in magnitude but appear smaller on a logarithmic scale.

VIII. SHOCK WAVE EXPERIMENTS

Dynamic shock compression experiments are the preferred laboratory experiments to probe the properties of materials at high pressure and temperature. Lasers[21], magnetic fields[11], and explosives[64] have recently been used to generate shock waves that reached megabar pressures. Under shock compression, the initial state of a material characterized by internal energy, pressure, and volume (E_0, P_0, V_0) changes to the final state described by (E, P, V). The conservation of mass, momentum, and energy yields the Hugoniot condition[65],

$$H = (E - E_0) + \frac{1}{2}(P + P_0)(V - V_0) = 0. \tag{12}$$

Different shock velocities lead to a collection of final states that are described by a Hugoniot curve. Using Eq. 12, this curve can easily be calculated for a given EOS where one most often may assume $P_0 \ll P$. $V_0 = 32.4$ cm^3/mol ($\rho_0 = 0.1235$ g cm^{-3}) is taken from experiment[19]. For E_0, one takes the energy of an isolated helium atom, which must be calculated consistently with the final internal energy, E. An initial static precompression that changes V_0 will also affect E_0 and P_0 but the corrections are negligible as long as the amount of initial compression work is small compared to the energy that is deposited dynamically. Assuming $dE_0 = dP_0 = 0$,

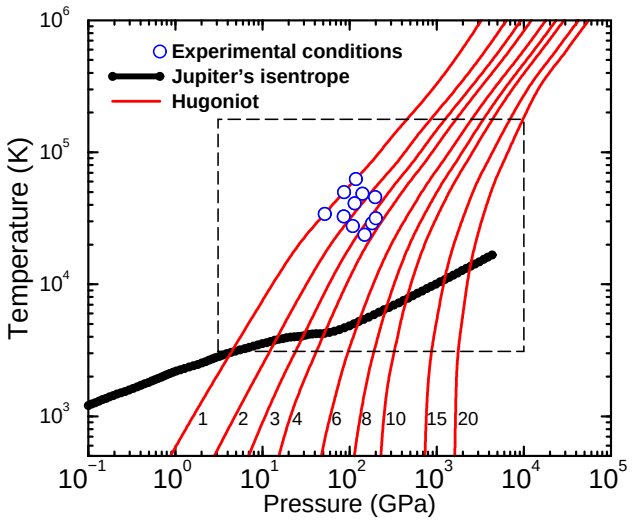

FIG. 17: Comparison of Jupiter's isentrope with helium shock Hugoniot curves for different precompression ratios. The labels specify the precompression ratio relative to the density at ambient pressures ($\rho_0 = 0.1235$ g cm^{-3}, Ref.[19]). The symbols approximately represent recent experiments[21]. The inside of the dashed box indicates conditions, for which the SCvH EOS[56] was interpolated and is not thermodynamically consistent.

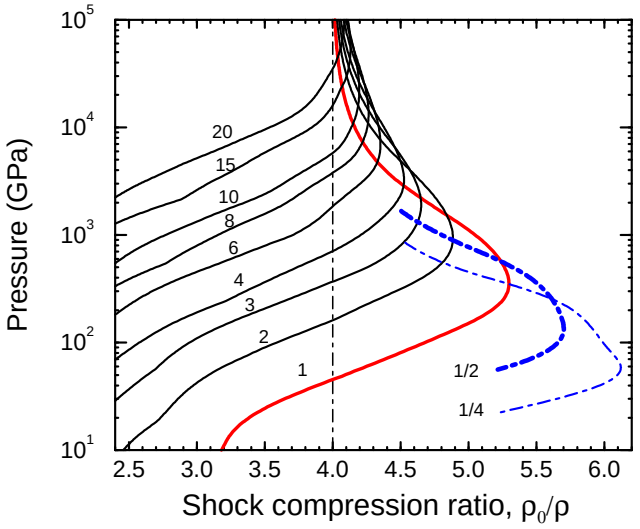

FIG. 18: Hugoniot curves for different precompression ratios from Fig. 17 plotted as function of shock compression.

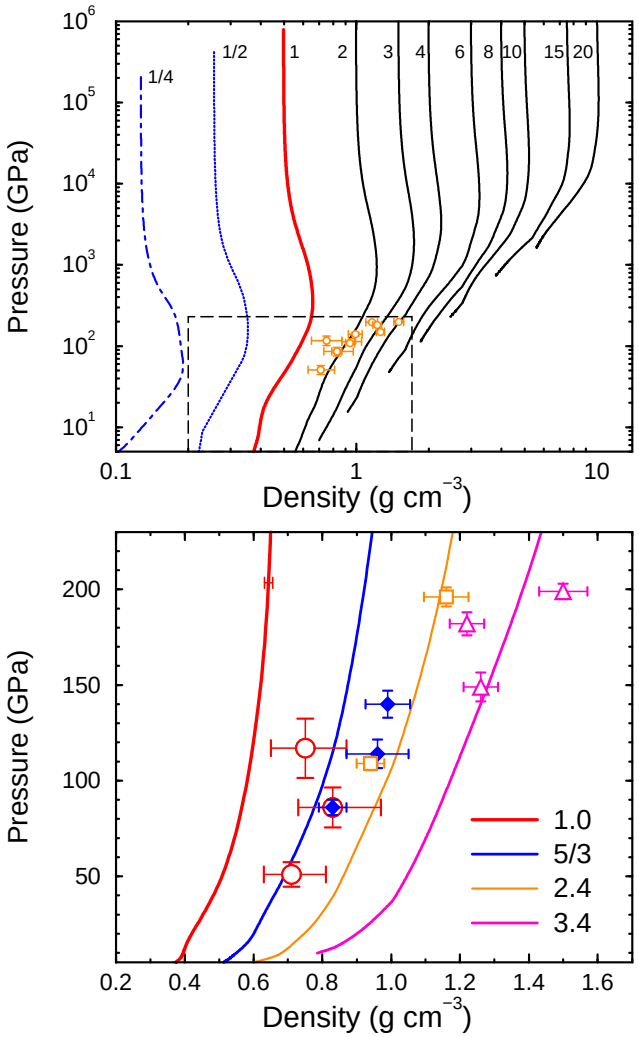

FIG. 19: Pressure-density plot of shock Hugoniot curves for different precompression ratios. The upper panel shows the shock Hugoniot curves from Fig. 18, recent experimental results (symbols), and the range of the lower plot. Below we plot the Hugoniot curves for precompression ratios (see labels) that approximately match the experimental conditions (symbols, see Ref.[21]). The error bar on the upper left solid line represents the uncertainty in the calculations.

the total differential of H reads,

$$dH = dE + \frac{P}{2}dV - \frac{P}{2}dV_0 + \frac{1}{2}(V - V_0)dP \qquad (13)$$

The point of maximum compression, $\eta_{\max} = V_0/V$, along the Hugoniot curve can be derived by setting, $dH = dV = dV_0 = 0$. The resulting condition can be expressed in terms of the Grüneisen parameter, $\gamma \equiv V \left.\frac{\partial P}{\partial E}\right|_V = 2/(\eta_{\max} - 1)$.

Now we will determine how the maximum compression ratio, $\eta_{\max}$, changes if the sample is precompressed statically. Keeping the final shock pressure constant, the compression ratio changes as function of the initial sample volume, V_0,

$$\left.\frac{\partial \eta}{\partial V_0}\right|_P = \frac{1}{V} - \frac{V_0}{V^2}\left.\frac{\partial V}{\partial V_0}\right|_P . \qquad (14)$$

Setting $dH = dP = 0$ in Eq. 13, one finds,

$$\left.\frac{\partial V_0}{\partial V}\right|_P = \frac{2}{P}\left.\frac{\partial E}{\partial V}\right|_P + 1 \equiv \frac{2}{\delta} + 1 . \qquad (15)$$

Inserting this result into Eq. 14 yields,

$$V \left.\frac{\partial \eta_{\max}}{\partial V_0}\right|_P = \frac{2(\gamma - \delta)}{\gamma(2 + \delta)} . \qquad (16)$$

Since the parameters γ and δ are both positive, the relation, $\left.\frac{\partial \eta_{\max}}{\partial V_0}\right|_P > 0$, is equivalent to the relation, $\delta < \gamma$, which is again equivalent to,

$$1 < \frac{\rho}{P}\left.\frac{\partial P}{\partial \rho}\right|_E . \qquad (17)$$

If this condition is fulfilled for a particular EOS then the maximum shock compression ratio will decrease if the sample is precompressed statically, which reduces V_0. We have computed the isoenergetic compressibility for our first-principles EOSs for helium and hydrogen and verified that this condition is satisfied for both materials (Fig. 18). It is also fulfilled for an ideal plasma model because the maximum compression ratio is determined by the balance of excitations of internal degrees of freedom and interaction effects[20]. Although all interactions are neglected, an ideal model correctly represents the fact that excited states are suppressed at high density because of the reduced entropy. The diminished importance of excitations reduces the maximum compression ratio to values closer to 4, which is the expected result for non-interacting systems without internal degrees of freedom.

Recent laser shock wave experiments[21] reached pressures of 2 megabars in fluid helium for the first time. The sample was precompressed statically in a modified diamond anvil cell before the shock was launched. The static precompression is an important development that enables one to reach higher densities and still allows one to directly determine the EOS. Reaching higher densities is important for planetary interiors because shock Hugoniot curves rise faster than adiabats in a P-T diagram like that shown in Fig. 17. As a result, a large part of Jupiter's adiabat remains inaccessible unless one increases the starting density by precompression. The precompression and relation of planetary interiors was studied theoretically in Ref.[66]. It was demonstrated that precompression of up to 60 GPa would be needed to characterize 50% of Jupiter's envelope. The challenge here is to reach high enough densities because a single shock wave compresses the material only 5.25-fold or less (Fig. 18).

The measurements of J. Eggert *et al.*[21] confirmed two of our theoretical predictions[20]. They showed that helium has a shock compression ratio substantially larger

than 4 due to thermal electronic excitations and that the compression ratio would decrease with increasing precompression (Fig. 18).

Figure 19 shows a detailed comparison between experiments and our first-principles simulations. The shock measurements without precompression show a higher compression than predicted from first principles. The deviations are outside the experimental and theoretical error bars. However, this discrepancy goes away with increasing precompression. The shocks with 3.4-fold precompression are in good agreement with first-principles predictions. We have no explanation for this trend at present. More experimental and theoretical work will be needed to reveal the reason for this discrepancy. Using our first-principles EOS, we converted the reported P-ρ measurements to temperature (see Fig. 17). Since the resulting shock temperatures span the interval of 24 000 – 63 000 K, the comparison with our EOS rests on DFT-MD.

In this temperature interval, the SCvH EOS predicts significantly lower pressures than our first-principles EOS (see Fig. 7). Consequently, this model predicts a higher compressibility for shock Hugoniot curves with and without precompression. As a result, the SCvH model agrees better than our first-principles calculations with those shock measurements that did not use any precompression. However, SCvH model is not in agreement with shock measurements that used precompressions more than 2-fold[21]. For those, it predicts a compressibility that is higher than measured.

Furthermore, it turns out that all measurements fall into the region where thermodynamic inconsistencies in the SCvH EOS model are large (see Fig. 17) and the model is expected to be less reliable than elsewhere. A different chemical model based on an expansion of the activity[67] predicts maximum compression ratios between 5.6 and 6.2 to occur at about 100 GPa, which is in good agreement with shock measurements without precompression.

IX. CONCLUSIONS

This work combined path integral Monte Carlo and density functional molecular dynamics simulations to derive one coherent equation of state for fluid helium at high pressure and temperature. Helium is a comparatively simple material since it does not form chemical bonds nor has core electrons, but our approach of combining two simulation techniques can be generalized to study more complex materials at extreme conditions. Certainly the presented approach to fitting the free energy and to deriving adiabats works for any set of EOS data points derived from first-principles simulations.

For the future, one might consider replacing DFT-MD with coupled ion-electron Monte Carlo[68]. However this is strictly a groundstate method and one would still need to find a way to include thermal electronic excitations.

Acknowledgments

This material is based upon work supported by NASA and NSF. We thank D. Saumon for providing us with his He EOS table[56], and acknowledge receiving the preliminary manuscript[24] from L. Stixrude and R. Jeanloz. We thank A. Sarid for comments and the authors of Ref.[21] for sending us a table with their experimental results.

[1] D.J. Stevenson and E.E. Salpeter. *Astrophys. J. Suppl. Ser.*, 35:221, 1977.
[2] D.J. Stevenson and E.E. Salpeter. *Astrophys. J. Suppl.*, 35:239, 1977.
[3] H. K. Mao, R. J. Hemley, Y. Wu, A. P. Jephcoat, L. W. Finger, C. S. Zha, and W. A. Bassett. *Phys. Rev. Lett.*, 60:2649, 1988.
[4] P. Loubeyre, R. LeToullec, J. P. Pinceaux, H. K. Mao, J. Hu, and R. J. Hemley. *Phys. Rev. Lett.*, 71:2272, 1993.
[5] D. A. Young, A. K. McMahan, and M. Ross. *Phys. Rev. B*, 24:5119, 1981.
[6] P. M. Kowalski, S. Mazevet, D. Saumon, and M. Challacombe. *Phys. Rev. B*, 76:075112, 2007.
[7] S. A. Khairallah and B. Militzer. *Phys. Rev. Lett.*, 101:106407, 2008.
[8] I. B. Da Silva, P. Celliers, G. W. Collins, K. S. Budil, N. C. Holmes, W. T. Jr. Barbee, B. A. Hammel, J. D. Kilkenny, R. J. Wallace, M. Ross, R. Cauble, A. Ng, and G. Chiu. *Phys. Rev. Lett.*, 78:483, 1997.
[9] G. W. Collins, L. B. Da Silva, P. Celliers, D. M. Gold, M. E. Foord, R. J. Wallace, A. Ng, S. V. Weber, K. S. Budil, and R. Cauble. *Science*, 281:1178, 1998.
[10] M. D. Knudson, D. L. Hanson, J. E. Bailey, C. A. Hall, J. R. Asay, and W. W. Anderson. *Phys. Rev. Lett.*, 87:225501, 2001.
[11] M. D. Knudson, D. L. Hanson, J. E. Bailey, C. A. Hall, and J. R. Asay. *Phys. Rev. Lett.*, 90:035505, 2003.
[12] S.I. Belov, G.V. Boriskov, A.I. Bykov, R.I. Il'kaev, N.B. Luk'yanov, A.Y. Matveev, O.L. Mikhailova, V.D. Selemir, G.V. Simakov, R.F. Trunin, I.P. Trusov, V.D. Urlin, V.E. Fortov, and A.N. Shuikin. *JETP Lett.*, 76:443, 2002.
[13] G. V. Boriskov, A. I. Bykov, R. I. Il'kaev, V. D. Selemir, G. V. Simakov, R. F. Trunin, V. D. Urlin, A. N. Shuikin, and W. J. Nellis. *Phys. Rev. B*, 71:092104, 2005.
[14] T. J. Lenosky, J. D. Kress, and L. A. Collins. *Phys. Rev. B*, 56:5164, 1997.
[15] B. Militzer and D. M. Ceperley. *Phys. Rev. Lett.*, 85:1890, 2000.
[16] N.C. Holmes, M. Ross, and W.J. Nellis. *Phys. Rev. B*, 52:15835, 1995.
[17] M. P. Desjarlais. *Phys. Rev. B*, 68:064204, 2003.
[18] S. A. Bonev, B. Militzer, and G. Galli. *Phys. Rev. B*, 69:014101, 2004.
[19] W. J. Nellis, N. C. Holmes, A. C. Mitchell, R. J. Trainor,

G. K. Governo, M. Ross, and D. A. Young. *Phys. Rev. Lett.*, 53:1248, 1984.
[20] B. Militzer. *Phys. Rev. Lett.*, 97:175501, 2006.
[21] J. Eggert, S. Brygoo, P. Loubeyre, R. S. McWilliams, P. M. Celliers, D. G. Hicks, T. R. Boehly, R. Jeanloz, and G. W. Collins. *Phys. Rev. Lett.*, 100:124503, 2008.
[22] A. Kietzmann, B. Holst, R. Redmer, M. P. Desjarlais, and T. R. Mattsson. *Phys. Rev. Lett.*, 98:190602, 2007.
[23] V. Ya. Ternovoi et al. *AIP Conf. Proc.*, 620:107, 2002.
[24] L. Stixrude and R. Jeanloz. *Proc. Nat. Ac. Sci.*, 105:11071, 2008.
[25] B. Militzer, W. H. Hubbard, J. Vorberger, I. Tamblyn, and S. A. Bonev. *Astrophys. J. Lett.*, 688:L45, 2008.
[26] N. Nettelmann, B. Holst, A. Kietzmann, M. French, R. Redmer, and D. Blaschke. *Astrophys. J.*, 683:1217, 2008.
[27] D. M. Ceperley. *Rev. Mod. Phys.*, 67:279, 1995.
[28] E. L. Pollock. *Comp. Phys. Comm.*, 52 :49, 1988.
[29] V. Natoli and D. M. Ceperley. *J. Comp. Phys.*, 117:171–178, 1995.
[30] B. Militzer and R. L. Graham. *Journal of Physics and Chemistry of Solids*, 67:2143, 2006.
[31] W. M. Foulkes, L. Mitas, R. J. Needs, and G. Rajagopal. *Rev. Mod. Phys.*, 73:33, 2001.
[32] N. D. Drummond, P. Lopez Rios, A. Ma, J. R. Trail, G. G. Spink, M. D. Towler, and R. J. Needs. *J. Chem. Phys.*, 124:224104, 2006.
[33] P. Lopez-Rios, A. Ma, N. D. Drummond, M. D. Towler, and R. J. Needs. *Phys. Rev. E*, 74:066701, 2006.
[34] M. Bajdich, L. Mitas, L. K. Wager, and K. E. Schmidt. *Phys. Rev. B*, 77:115112, 2008.
[35] D. M. Ceperley. *J. Stat. Phys.*, 63:1237, 1991.
[36] D. M. Ceperley. Editrice Compositori, Bologna, Italy, 1996.
[37] B. Militzer and E. L. Pollock. *Phys. Rev. E*, 61:3470, 2000.
[38] CPMD, Copyright IBM Corp 1990-2006, MPI für Festkörperforschung Stuttgart 1997-2001.
[39] N. Troullier and J. L. Martins. *Phys. Rev. B*, 43:1993, 1991.
[40] G. Kresse and J. Hafner, Phys. Rev. B 47, 558 (1993); G. Kresse and J. Hafner, Phys. Rev. B 49, 14251 (1994); G. Kresse and J. Furthmüller, Comput. Mat. Sci. 6, 15 (1996); G. Kresse and J. Furthmüller, Phys. Rev. B 54, 11169 (1996).
[41] P. E. Blöchl. *Phys. Rev. B*, 50:17953, 1994.
[42] J. P. Perdew, K. Burke, and M. Ernzerhof. *Phys. Rev. Lett.*, 77:3865, 1996.
[43] N. D. Mermin. *Phys. Rev.*, 137:A1441, 1965.
[44] R.A. Aziz, A.R. Janzen, and M. R. Moldover. *Phys. Rev. Lett.*, 74:1586, 1995.
[45] E. L. Pollock and B. Militzer. *Phys. Rev. Lett.*, 92:021101, 2004.
[46] B. Militzer and E. L. Pollock. *Phys. Rev. B*, 71:134303, 2005.
[47] G. S. Stringfellow, H. E. DeWitt, and W. L. Slattery. *Phys. Rev. A*, 41:1105, 1990.
[48] B. Militzer and D. M. Ceperley. *Phys. Rev. E*, 63:066404, 2001.
[49] E. A. Hylleraas. *Z. Phys.*, 54:347, 1929.
[50] A. A. Bürgers, D. Wintgen, and J.-M. Rost. *J. Phys. B*, 28:3163, 1995.
[51] G. Tanner, K. Richter, and J.-M. Rost. *Rev. Mod. Phys.*, 72:497, 2008.
[52] O. H. Nielsen and R. M. Martin. *Phys. Rev. B*, 32:3780, 1985.
[53] P. Debye and E. Hückel. *Phys. Z.*, 24:185, 1923.
[54] L. D. Landau and E. M. Lifshitz. *Statistical Physics*. Pergamon Press New York, 1969.
[55] C. Winisdoerffer and G. Chabrier. *Phys. Rev. E*, 71:026402, 2005.
[56] D. Saumon, G. Chabrier, and H. M. Van Horn. *Astrophys. J. Suppl.*, 99:713, 1995.
[57] Q. Chen, Y. Zheng, L. Cai, Y. Gu, and F. Jing. *Phys. Plasmas*, 14:012703, 2007.
[58] A. Förster, T. Kahlbaum, and W. Ebeling. *Laser Part. Beams*, 10:253, 1992.
[59] D. Saumon and G. Chabrier. *Phys. Rev. A*, 46:2084, 1992.
[60] B. Militzer and W. H. Hubbard. in press *Astrophys. and Space Sci., arXiv astro-ph/0807.4266*, 2008.
[61] B. Militzer. *J. Phys. A,* in press, 2008, cond-mat: 0902.4281.
[62] T. J. Lenosky, S. R. Bickham, J. D. Kress, and L. A. Collins. *Phys. Rev. B*, 61:1, 2000.
[63] W. H. Press, S. A. Teukolsky, W. T. Vetterling, and B. P. Flannery. *Numerical Recipes in C++*. Cambridge University Press, Cambridge, UK, 2001.
[64] V. E. Fortov, R. I. Ilkaev, V. A. Arinin, V. V. Burtzev, V. A. Golubev, I. L. Iosilevskiy, V. V. Khrustalev, A. L. Mikhailov, M. A. Mochalov, V. Ya. Ternovoi, and M. V. Zhernokletov. *Phys. Rev. Lett.*, 99:185001, 2007.
[65] Y. B. Zeldovich and Y. P. Raizer. Academic Press, New York, 1966.
[66] B. Militzer and W. B. Hubbard. *AIP Conf. Proc.*, 955:1395, 2007.
[67] M. Ross, F. Rogers, N. Winter, and G. Collins. *Phys. Rev. B*, 76:020502(R), 2007.
[68] K. T. Delaney, C. Pierleoni, and D. M. Ceperley. *Phys. Rev. Lett.*, 97:235702, 2006.

Appendix A: Free energy spline interpolation

We constructed the following 2D spline interpolation of the free energy in order to reproduce the internal energy and pressures from Tab. I. We use atomic units of Hartrees and Bohr radii. For each density of $r_s = \{2.4, 2.0, 1.6, 1.2, 0.8\}$, we construct a cubic spline $F_n(T)$. Table VI lists 16 knot points $(T_i, F(T_i))$ for each density. In addition, the first derivate $\frac{\partial F}{\partial T}$ are specified at the lowest and highest temperatures. This is sufficient to construct a cubic spline function $F(T)$[63].

In a similar fashion, we derive a spline function that contains that free energy derivative with respect to density, $\frac{\partial F}{\partial n}(T)$, at the lowest and highest densities, $r_s = 2.4$ and 0.8 respectively. n is the density of the electrons, $n = N_e/V$. Those knot points as well as the T derivatives are included in Tab. VI also.

In order to obtain the free energy for a particular density and temperature, (n^*, T^*), we proceed as follows. First we evaluate the spline functions $F(T^*)$ and $\frac{\partial F}{\partial n}(T^*)$ at temperature T^*. Using these five knots points and density derivatives, we construct a spline function, $F(\log(n))$. We use $\log(n)$ as argument because it better represents the high-temperature limit of weak interactions. Note that the constructed splines for the density

derivate contain $\frac{\partial F}{\partial n}$ and not $\frac{\partial F}{\partial \log(n)}$. Then $F(\log(n))$ is evaluated at the density of interest, n^*. Finally we add the term, $-T\Delta S = -13.7902836$ Ha$^*T$, which brings the entropy in agreement with our Debye-Hückel reference point at high temperature for r_s=1.86. This procedure yields the free energy $F(n^*, T^*)$ in Hartrees per electron. Other thermodynamic variables including pressure, internal energy, entropy, and Gibbs free energy can be obtained by differentiation.

TABLE VI: Knot points for free energy spline interpolation

T(a.u.)	$f(r_s=2.4,T)$	$f(r_s=2.0,T)$	$f(r_s=1.6,T)$	$f(r_s=1.2,T)$	$f(r_s=0.8,T)$
0.001583407607	-1.433567121	-1.431135811	-1.422237604	-1.377317056	-1.089747214
0.004369348882	-1.406243368	-1.402248169	-1.390358674	-1.34121764	-1.049220122
0.01205704051	-1.338444742	-1.330719999	-1.313137294	-1.255091313	-0.9491949603
0.03327091284	-1.169814789	-1.154154406	-1.125146478	-1.047701304	-0.7135001905
0.09180973061	-0.7578793569	-0.7214892496	-0.6653645937	-0.5501514183	-0.1583196636
0.2533452171	0.1213432393	0.2279596473	0.3697481593	0.5961317377	1.145222958
0.6990958211	1.448161918	1.849742465	2.331720062	2.967152398	4.011622282
1.929126481	1.650153009	3.082886945	4.795803813	6.956651264	9.947352284
5.323346054	-6.480107758	-2.223161966	2.964697691	9.579180258	18.74636894
14.6895569	-50.37972679	-38.41515844	-23.79211621	-4.992619324	21.39894481
40.53523473	-231.4313924	-198.2806566	-157.6765535	-105.3657984	-31.61456362
111.8553314	-893.7314032	-802.1449141	-689.7861073	-544.9061891	-340.7935545
308.660237	-3172.519712	-2918.919455	-2608.696846	-2207.77895	-1644.63782
851.7353686	-10693.37579	-9996.590015	-9137.681211	-8032.176108	-6477.239292
2350.329104	-34893.6373	-32971.41578	-30600.55572	-27552.36594	-23259.81241
6485.637557	-111050.5942	-105746.9466	-99203.62441	-90788.1102	-78945.99564
$f'(r_s,T_1)$	10.43646526	10.93007841	12.42958105	14.04097874	13.75171132
$f'(r_s,T_N)$	-19.3620206	-18.54727965	-17.53417624	-16.23883073	-14.41224513

T(a.u.)	$\frac{\partial f}{\partial n}(r_s=2.4,T)$	$\frac{\partial f}{\partial n}(r_s=0.8,T)$
0.001583407607	0.1605721538	0.9460950728
0.004369348882	0.2923651353	0.9625433841
0.01205704051	0.6458549976	0.9782855175
0.03327091284	1.463747273	1.029890765
0.09180973061	3.574255133	1.142591093
0.2533452171	10.98479122	1.409424435
0.6990958211	43.27443042	2.089943658
1.929126481	153.211445	5.309130852
5.323346054	450.4159975	15.9843674
14.6895569	1263.720981	46.33079487
40.53523473	3502.359609	129.8984992
111.8553314	9679.619949	359.8256334
308.660237	26719.83852	992.5003633
851.7353686	73736.1465	2741.461026
2350.329104	203474.5198	7568.332998
6485.637557	561480.8894	20879.15481
$f'(r_s,T_1)$	47.35562925	6.453623893
$f'(r_s,T_N)$	86.57538487	3.218499127

TABLE VII: Reduced coordinates of the DFT-MD configuration with 57 atoms that was used to report the $r_s = 1.86$ results for the instantaneous pressure in Fig. 4. The cell size is $L = 14.5382$ a.u.

x/L	y/L	z/L	x/L	y/L	z/L
0.749029	0.334272	0.723992,	0.359050	0.631169	0.090795
0.636183	0.917961	0.531890,	0.500277	0.715818	0.420142
0.509121	0.642554	0.328933,	0.192192	0.222632	0.042651
0.273631	0.845722	0.363632,	0.070837	0.830223	0.693497
0.053785	0.837401	0.054990,	0.138489	0.091713	0.097622
0.250609	0.517490	0.740851,	0.953625	0.430789	0.067921
0.107008	0.407958	0.463387,	0.023708	0.960709	0.487179
0.988548	0.830572	0.241931,	0.811738	0.062550	0.902069
0.244399	0.482412	0.399190,	0.693258	0.647174	0.360832
0.924284	0.678572	0.470508,	0.181701	0.886709	0.333868
0.780287	0.033015	0.620919,	0.859185	0.932541	0.252564
0.774645	0.083064	0.349744,	0.903457	0.888628	0.124621
0.293881	0.081041	0.053630,	0.220134	0.760599	0.688370
0.493690	0.930407	0.343378,	0.585411	0.439278	0.167284
0.648043	0.965342	0.702852,	0.219455	0.957094	0.895428
0.504966	0.639074	0.084498,	0.906610	0.508304	0.938057
0.716468	0.854022	0.986517,	0.385839	0.307391	0.681601
0.099368	0.291429	0.740170,	0.475139	0.160612	0.598743
0.252564	0.696499	0.576596,	0.788211	0.564812	0.486616
0.613177	0.259980	0.238984,	0.296858	0.344416	0.229757
0.526564	0.816547	0.598836,	0.429733	0.712523	0.742929
0.507514	0.904602	0.268688,	0.685066	0.562001	0.926251
0.614731	0.263859	0.402947,	0.432246	0.210193	0.939664
0.115992	0.498747	0.676389,	0.424152	0.141821	0.676522
0.778767	0.981750	0.935757,	0.208696	0.768371	0.292528
0.334815	0.183086	0.275601,	0.487257	0.590889	0.227333
0.975542	0.456665	0.257836,	0.577884	0.835181	0.876629
0.737370	0.699890	0.544111,	0.177496	0.781162	0.853225
0.558513	0.066648	0.194491			